Doctoral Dissertation

Multiscale Relative Nonlinearity in High-Resolution Forecasts for a Mesoscale Convective System

メソ対流系の高解像度予測における多重スケールの相対的非線形性

Kosuke Ono

小野　耕介

Division of Earth and Planetary Dynamics, Department of Natural History Sciences,

Graduate School of Science, Hokkaido University

北海道大学大学院理学院自然史科学専攻

地球惑星ダイナミクス講座

2024 年 9 月

Abstract

Modern weather forecasting necessitates numerical model simulations on supercomputers. Because numerical forecast models represent full atmospheric dynamics and physics with spatiotemporal discretization and parametrizations, their simulated results generally exhibit a chaotic behavior, making the forecasts sensitive to initial conditions. Operational forecast centers recently introduced ensemble forecasts to generate many possible forecasts by running the model from initial conditions perturbed around the most likely states. The initial perturbations are expected to grow significantly over time to lead to a wide range of possible forecast. They have been practically determined by approximating finite-time local Lyapunov vectors. Because ensemble forecasts by a low-resolution global model reasonably assume that perturbations evolve linearly over a specific period, the initial perturbations are typically prepared as a pair of states with equal magnitude but opposite signs. The pair of initial perturbations grow in opposite directions, allowing them to represent the range of forecast until the linear assumption satisfies. However, it remains uncertain whether the linear assumption holds in high-resolution mesoscale forecasts, particularly under atmospheric states characterized by multiscale phenomena.

This dissertation aims to explore detailed behavior in ensemble forecasts using a high-resolution mesoscale model when the initial opposite-sign perturbed state is provided in an event where the multiscale phenomena prominently present. A pair of 18-h forecast experiments with initial perturbations of different signs was conducted for a heavy rainfall event along with the shear zone on the persistent Baiu front in western Japan on 13 August 2021. Despite the initially different signs, the perturbations had random structures at convective scales over 2 h as previous studies have shown. However, the perturbations had the same sign on the meso-α scale at 11 h. This result suggested that the nonlinear signal was found not only on the convective scale but also

on the meso-α scale. Additional experiments showed that this meso-α scale nonlinear signal originated from the front with high convective activities in the initial field through the emission of gravity waves via the moist physics.

日本語要旨

現代の天気予報は大型計算機上において数値予報モデルを実行する必要がある．数値予報モデルは時空間における離散化とパラメタリゼーションによって大気力学の物理過程を表現するためカオス的な振る舞いを示し，予報は初期値鋭敏性を持つ．このため，多くの現業気象センターではアンサンブル予報を導入し，最尤値である決定論的初期値を摂動させた複数の初期値から数値予報モデルを実行することで、将来起こり得る予報を複数生成している．初期摂動は時間の経過とともに大きく成長することで起こり得る予報の幅を捉えることが期待される．この初期摂動は有限時間局所リアプノフベクトルを近似することによって実用的に計算される。低解像度の全球モデルによるアンサンブル予報では，摂動が一定期間に渡って線形的に時間発展することを仮定するため，初期値摂動は通常，大きさは等しいが符号が反対の一対の状態として用意される．一対の初期摂動は反対方向に時間発展するため，線形的な時間発展を示す限り，予測の幅を表現することができる．一方，対流を表現する高解像度の数値予報モデルを用いた研究では，メソスケールの予測、特に多重スケールの構造を持つ大気に対して，摂動の線形近似が妥当かどうかは明らかではない．

本論文では，高解像度数値予報モデルを用いたアンサンブル予報において，マルチスケールの現象が顕著に現れる事例を対象に，符号の異なる初期摂動を与えた場合の初期摂動の詳細な挙動を探ることを目的とする．2021 年 8 月 13 日に発生した西日本の梅雨前線上の豪雨に対して，符号の異なる初期摂動から 18 時間の予報実験を行った．その結果，符号の異なる初期摂動にもかかわらず，これまでの研究で示されているように，対流規模では摂動は予報開始からわずか 2 時間でランダムな構造へと変化した．一方，メソ α スケールにおいても予報開始から 11 時間後には同様の構造を持つことが示された．この結果は，この非線形シグナルが対流規模だけでなく，メソ α スケールでも見られることを示している．また，このメソ α スケールの非線形なシグナルは，初期場において対流活動が活発な前線から湿潤過程を通じて重力波が放出され，それに由来するものであることが示された．

Table of contents

Chapter 1. Introduction

Modern weather forecasting has advanced with progress in meteorology and computer technology. After the pioneering work by Charney and von Neumann (Charney et al. 1950), global weather forecast has been operationally realized through meteorological models since the 1950s (e.g. Persson 2006). Global models have been much improved to provide a better performance in daily-to-weekly forecasts by including sophisticated paramatrizations such as radiation, convection, and boudary-layer turnulence and by advancing the discretization technique. Computational advancements have made it possible to achieve higher resolution forecasts using global models. Moreover, daily weather forecasts with O(10 km) resolution were succeeded in the 1970s by limited area models imposing lateral boundary conditions. Nowadays, the resolution of operational global models reached O(10 km), and that of regional models is approaching O(1 km).

On the other hand, since Lorenz (1963) found the atmospheric chaotic behavior inhenrent in the model system, the numerical forecasts have suffered from the amplification of errors from an initial conditon. Therefore, even slight differences in initial states can often lead to significantly different outcomes within a finite lead time. The idea that the forecast from multiple initial values offered the range of possible states at a future time was advocated by Epstein (1969). In the early stage of the ensemble forecast research, initial conditions were randomly perturbed (Leith 1974). The operational centers readily adopted lagged average forecast, in which initial perturbations were generated based on forecast results starting from a past time (Hoffman and Kalnay 1983). These methods, however, were hindered by the problem that the forecasts from different initial condition sometimes exhibited insufficient variety at a lead time, making it difficult to evaluate the forecast uncetainty.

According to the local Lyapunov analysis in the dynamical system, the initial perturbation that sufficiently spreads should be the most growing state vector from the infinite past. We regard a forecast model as a dynamical system and evaluate the most optimal initial perturbations within a finite time that approximate a set of the local Lyapunov vectors for a particular atmospheric state. The breeding of growing mode (BGM; Toth and Kalnay 1993) and the singular vector (SV; Lorenz 1965) were used as standard methods in ensemble forecasting by operational centers such as European Centre for Medium-Range Weather Forecasts (Buzza and Palmer 1995) and the National Center for Environmental Prediction (Toth and Kalnay 1997). They generate initial perturbations that exhibit an effective growth in time. The operational centers conventionally provided an initial perturbation obtained by SV or BGM methods and the other one with its opposite directon to based on a growing vector at the initial time and evolves with time keeping its opposite patterns. Asuuming that the initial perturbations grew linearly, a pair of initial perbertions would indicate a possible range of growth along their direction. Hence, if the model were perfect, some pairs of initial perturbations would be expected to grow, forming an ellipsoidal domain that effectively captures almost all possible forecast states.

An ensemble forecast has been recently introduced in short-term weather forecasting to offer practical predictability information (e.g. Kühnlein et al. 2014; Raynaud and Bouttier 2017; Ono et al. 2021). Assuming that the initial perturbations grow linearly in time, a pair of opposite-sign initial perturbations is also routinely input into a synoptic forecast system to generate as many forecast varieties as possible, similarly to global ensemble prediction[1] (e.g., Wang et al. 2014; Ono et al. 2021). However, Hohenegger and Schär (2007a) demonstrated that runs with different initial perturbations imposed in their cloud-resolving model provided similar spatial patterns of perturbations after 11 h. This result suggests that the mesoscale model forecast often

[1] Regional EPSs are also required lateral boundary perturbations different form global EPSs.

yielded nonlinear signals, where the forecast difference is not proportional to the initial signal within several hours. The nonlinear perturbation growth does not guarantee that a pair of initial perturbations reasonably exhibit a range of possible future states along with the growing direction.

This problem can be reframed in terms of the validity of the tangential linear approximation on mesoscale models. Ancel and Mass (2006) showed that it degraded with higher horizontal resolutions up to 24-km gridspacing for an extratropical cyclone event. Lang et al. (2012) also studied the dependancy of model resolution and diabatic process against the tangential linear approximation for a specific typhoon case. Demirdjian et al. (2020) investigated the validity of tangent linear apporoximation on precipitation forecast associated with the atmospheric river by using the mesoscale model with a 40 km-horizontal gridspacing. These studies showed that the tangent linear approximation is valid for mesoscale model with O(10 km) resolution.

A possible violation of tangential linear approximation in the mesoscale models appeared to be related to multiscale interactions. Research on perturbation magnitude upscaling in the initial perturbation growth experiments has also hinted at the expected nonlinear signals found in the mesoscale model forecast (e.g. Sun and Zhang 2016; Weyn and Durran 2017; Wu and Takemi 2023; Minamide et al. 2020). Zhang et al. (2007) attributed the fast growth of small-scale perturbations to convective instability over the first few forecast hours, whereas they attributed the slow growth of synoptic perturbations to baroclinic instability on a daily timescale. In mesoscale convective systems (MCSs), the meso-β scale (20–200 km) initial perturbation downscales rapidly, and then upscales (Durran and Weyn 2016). The upscale energy cascade through gravity wave excitation and resultant geostrophic adjustment may enlarge the convective-scale perturbation at the meso-γ scale (2–20 km) to the meso-β scale or even the meso-α scale (200–2000 km; Selz and Craig 2015), as suggested theoretically (Bierdel et al. 2017) or by idealized experiments (Bierdel et al. 2018). Rodwell et al. (2013) showed that the convective activity in the United States degraded the synoptic wave forecast in Europe through upscaling.

These studies highlight the importance of upscaling error growth from the convective scale; thus, the nonlinear signals in a mesoscale model forecast may be associated with a type of upscaling. Previous studies also showed that perturbation growth and its upscaling does matter in weather forecasts. However, it is unknown whether a pair of perturbations evolves lineary over time by using the high-resolution model which can resolve convections, and how the nonlinear signals, if any, are related to the upscaling processes from the convective scale to mesoscale.

The purpose of this study is to explore how the nonlinear signals associated with an MCS are related to the upscaling error growth from the convective scale by the detailed description of a pair of initial perturbations over several hours in a forecast. We adopted a high-resolution forecasting model to simulate the convective activities, and applied spatial filtering to the model perturbation at all forecast times to emphasize the upscaling of the perturbation structures with time at the mesoscale environment.We targeted an event on 13 August 2021 (Fig. 1.1), where heavy rainfall was associated with a line-shaped rainband, frequently observed in western Japan in the summertime Asian monsoon environment (Kato 2020; Hirockawa et al. 2020). We chose this event because the line-shaped rainband is an MCS that contains a multiscale structure, from the upper-level cold low to the lower-level water vapor flow (e.g., Kawano and Kawamura 2020). Moreover, this case was characterized by the strong convective activity related to the persistent line-shaped rainband diffent from the usual front-related rainfall events without a line-shaped rainband, which made us reasonable to analyze the upscaling processes from convective scale to mesoscale. We conducted a plausible set of initial perturbation growth experiments with an operational mesoscale forecast system of the Japan Meteorological Agency (JMA).

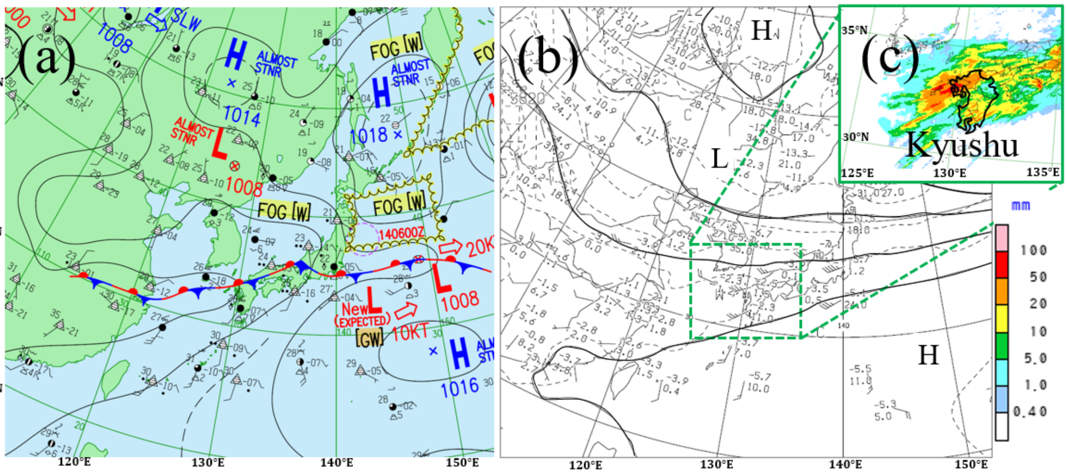

Fig. 1.1. (a) Japan Meteorological Agency (JMA) surface weather chart and (c) 3-h accumulated precipitation observed by Radar/Raingauge-Analyzed Precipitation data (R/A: JMA 2022) at 0600 UTC on 13 August 2021. (b) JMA's 500-hPa weather chart at 0000 UTC on 13 August 2021 showing geopotential height (black contours). In (c), the color shading is as per the reference in the right panel and the bold black line shows Kyushu Island.

The remainder of this paper is organized as follows. Chapter 2 describes the forecast model and the initial perturbation method used in this study. Chapter 3 explains the evaluation of nonlinear signals and spatial filtering. Chapter 4 presents the results on the nonlinear signals in the perturbations in our forecast experiments. Chapter 5 provides the summary of this studyand discusses the interpretation of the results. Chapter 6 gives the general conclusion of this study.

Chapter 2. Experimental settings

2.1. Model

As the regional forecast model, we used A System based on a Unified Concept for Atmosphere (ASUCA; Ishida et al. 2022), which is part of the JMA's operational forecasting system, as of May 2024. We set the model configuration as in the operational local forecast model (LFM) [See Table 3.1.3 of JMA 2022 for detailed specifications] with a horizontal grid spacing of 2 km, but the forecasting period was extended to 18 h. The time step was 12 seconds. The forecast domain was the whole region shown in Fig. 2.1a, which was composed of 1585 × 1305 horizontal grid points. The hybrid terrain-following vertical coordinate was adopted with 76 layers. The depth of vertical layers increased with height from 20 m at the lowest layer to about 650 m at the highest [See Fig. B1 of Ishida et al. (2022) for more details]. Rayleigh damping was adopted in 180 km from the lateral boundaries and in 7 km from the model top (~21,000 m). The model variables were output every hour.

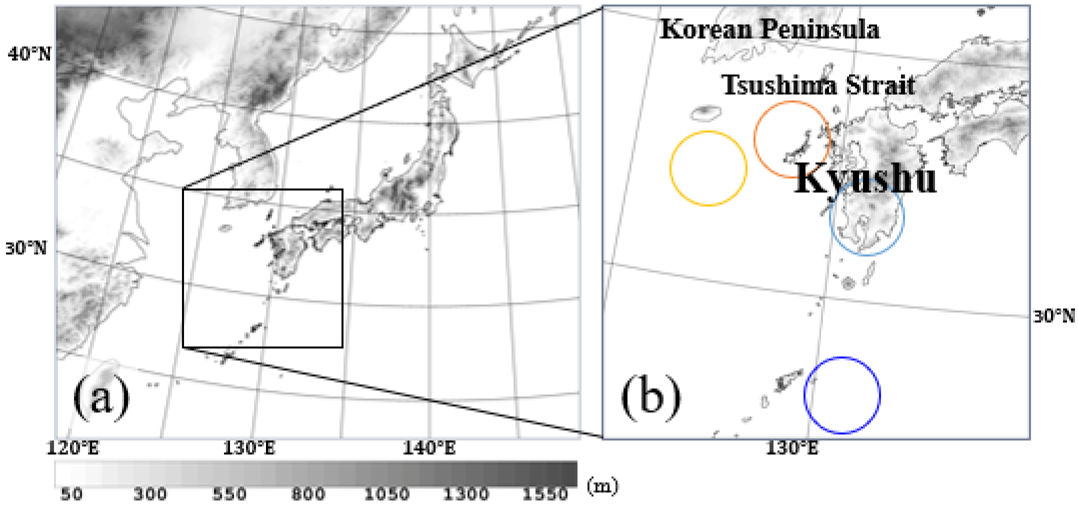

Fig. 2.1. Computational domain of LFM and its surface height above the sea level (a) and enlarged view around Kyushu (b). Circles in (b) indicate the initially perturbed areas for the initial perturbation sensitivity experiments, (yellow) pF and nF, (orange) pF' and nF', (blue) pS and nS, and (skyblue) pS' and nS' (detailed in Table 2.1).

The prognostic variables of ASUCA are total mass density, momentum, mass-virtual potential temperature, density of water vapor and water substances (cloud water, cloud ice, rain, snow, and graupel), ground temperature, soil water, and four of the second-order moments of turbulent fluctuation including turbulent kinetic energy. The planetary-boundary-layer mixing processes are simulated based on Mellor–Yamada–Nakanishi–Niino Level-3 scheme (Nakanishi and Niino 2009); and the surface flux is calculated based on Monin–Obukhov similarity theory (Beljaars and Holtslag 1991). Cloud physics was considered by the single-moment, three-ice bulk method (Ikawa and Saito 1991) based on Lin et al. (1983). Cumulus convection was then represented explicitly, except for the convection initiation (Hara 2015), which was parameterized based on the Kain-Fritsch scheme (Kain and Fritsch 1990; Kain 2004)[2].

---

[2] Hara (2015) showed that the LFM could not forecast lower-layer convergence smaller than the

Initial conditions for the LFM were generated by the three-dimensional variational data assimilation, which assimilates radial velocity and reflectivity from doppler radars to help the spin-up in convective regions (Ikuta et al. 2021). The lateral boundary conditions for the LFM were provided by the JMA's operational mesoscale model (Sawada et al. 2022) with a horizontal grid spacing of 5 km.

2.2. Initial perturbation

The initial perturbations were made by the breeding of growing mode method (Toth and Kalnay 1993), which sought a set of the perturbations with the greatest growth in the model run (Fig. 2.2a). This method conducts the forecast cycle (breeding cycle) with the initially perturbed forecast (breeding run) and the unperturbed forecast (control run) to extract the growing modes and dump the decaying modes in the perturbations. The whole forecast cycle is set until the bred vector has grown sufficiently in the whole forecast domain. The length of each forecast is set in

---

grid scale that triggers convection without cumulus convection parameterization, resulting in a delay in the initiation of convection. To address this issue, in the LFM, the vertical transport of heat, water vapor, and cloud water were parameterized in slightly unstable stratifications by activating the cumulus parameterization based on the Kain–Fritsch scheme (Kain and Fritsch 1990) at each timestep only for convective initiation. The effects of the parameterization on the forecast variables were weaker than those of the original Kain–Fritsch scheme (Hara 2015).

consideration of the duration of target phenomenon. In this study, the 54 h until the target event started, that is, the period from 0000 UTC 11 August 2021 to 0600 UTC 13 August, were allocated for the breeding process with its 6 h cycle (Fig. 2.2a), which is considered to the whole duration of single convective cell.

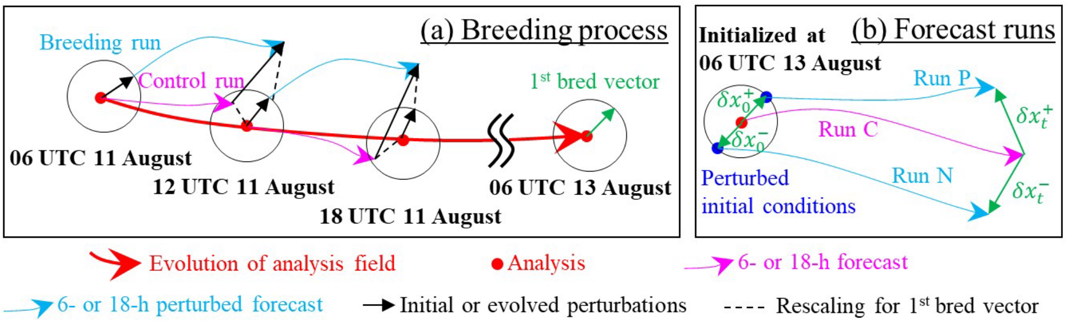

Fig. 2.2. Schematics of the (a) breeding process and (b) control and perturbed forecasts. Green arrow in (a) is the first bred vector, and the first bred vector in (a) was used in the perturbed runs in (b).

The procedures to extract the growing modes as a bred vector are as follows. First, we conducted the control run for 6 h. Next, the breeding run was conducted for 6 h with an unperturbed initial condition and a perturbed lateral boundary condition. The initial perturbations were not used at the start of the breeding cycle (Fig. 2.3a) but were created at 0600 UTC 11 August after the first breeding cycle (Fig. 2.3b). The breeding run was restarted from the rescaling state plus the control run's result at 6 h of breeding, and the model ran for the next 6 h. The difference between breeding and control runs at 6 h of breeding, for example, 1200 UTC 11 August in this case, was rescaled (broken lines in Fig. 2.2a; Fig. 2.3c) to a magnitude comparable to those in the degree of uncertainty for the JMA's current mesoscale model initial condition [horizontal wind ~ 1.8 m s^{-1}, temperature ~ 0.7 K, and water vapor mixing ratio ~ 1.0 g kg^{-1} after Ono et al. (2021)]. This procedure is to prevent the perturbation amplitude from divergence. By repeating this procedure for a further 54 h of breeding, we obtained the fastest-growing perturbation called "the first bred vector".

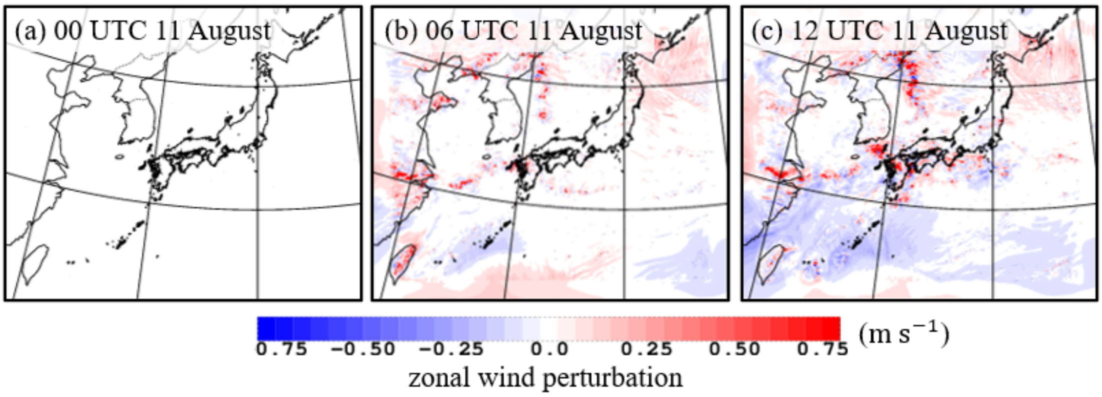

Fig. 2.3. Zonal wind component of bred vector (m s^{-1}) on the 21st model level at 0000 UTC (a), 0600 UTC (b) and 1200 UTC (c) on 11 August 2021.

The lateral boundary perturbations in the breeding cycle for horizontal wind, temperature, and water vapor mixing ratio were obtained from the JMA's global ensemble prediction system in advance (Ota et al. 2023). We did not calculate the lower boundary perturbations and physics perturbations in the above breeding cycle.

The rescaling and normalization in the breeding process require the norm and the associated inner product. We used the total energy norm for the perturbed state vector of $\boldsymbol{\delta x} = (\delta u\ \delta v\ \delta\theta\ \delta q\ \delta p_s)^{\mathbf{T}}$ over model domain S (Ehrendorfer et al. 1999) defined by

$$\|\boldsymbol{\delta x}\|_S^2 = \int_{z_1}^{z_2}\int_S \frac{\rho}{2}\left(\delta u^2 + \delta v^2 + \frac{C_p}{\Theta_r}\delta\theta^2 + \frac{RT_r}{P_r^2}\delta p_s^2 + \frac{L^2}{C_pT_r}\delta q^2\right) dS\, dz, \qquad (2.1)$$

where ρ is density; δu and δv are zonal and meridional wind perturbations, respectively; θ, δp_s, and δq are perturbations of potential temperature, surface pressure, and water vapor mixing ratio, respectively; $C_p = 1005.7\ \mathrm{J\ kg^{-1}\ K^{-1}}$ is the specific heat at constant pressure; $\Theta_r = 300\ \mathrm{K}$, $T_r = 300\ \mathrm{K}$, and $P_r = 10^5\ \mathrm{Pa}$ are the reference values of potential temperature,

temperature, and pressure, respectively; $R = 287.04\ \mathrm{J\ kg^{-1}\ K^{-1}}$ is the gas constant for dry air; and $L = 2.51 \times 10^6\ \mathrm{J\ kg^{-1}}$ is the latent heat of vaporization. We set z_1 as the lowermost model level and z_2 as the 53rd model level (~9500 m). The level z_2 was set to focusing on the phenomena in only troposphere. The associated inner product was also defined as

$$\|\boldsymbol{\delta x}\|_S^2 = \int_{z_1}^{z_2} \int_S \frac{\rho}{2} \left(\delta u^2 + \delta v^2 + \frac{C_p}{\Theta_r} \delta\theta^2 + \frac{RT_r}{P_r^2} \delta p_s^2 + \frac{L^2}{C_p T_r} \delta q^2 \right) dS\, dz, \tag{2.2}$$

for $\boldsymbol{\delta x_1} = \left(\delta u_1\ \delta v_1\ \delta\theta_1\ \delta q_1\ \delta p_{s,1}\right)^{\mathbf{T}}$ and $\boldsymbol{\delta x_2} = \left(\delta u_2\ \delta v_2\ \delta\theta_2\ \delta q_2\ \delta p_{s,2}\right)^{\mathbf{T}}$.

2.3. Forecast runs

We performed the control forecast run (run C) and 10 pairs of positive and negative initially perturbed forecast runs (Table 2.1). All forecasts were initialized at 0600 UTC on 13 August 2021 and run for 18 h without the lower and lateral boundary perturbations or physics perturbations (Fig. 2.2b). No perturbations from lateral boundaries affected the perturbation growth in domain K until the end of the forecast (not shown); thus, we only handled the initial perturbation growth in the whole forecast domain. The atmospheric flow around Japan was so slower in summer than in winter owing to the prevailing stronger jet streams that the lateral boundary did not affect the domain K in this case. Run C was performed with no initial perturbations over the model domain.

A pair of perturbed forecast runs were performed with the first bred vector added to the control's initial conditions. Because the sign of the perturbation was arbitrary, two opposite directions could be chosen in the first bred vector. We nominated one direction as run P and the

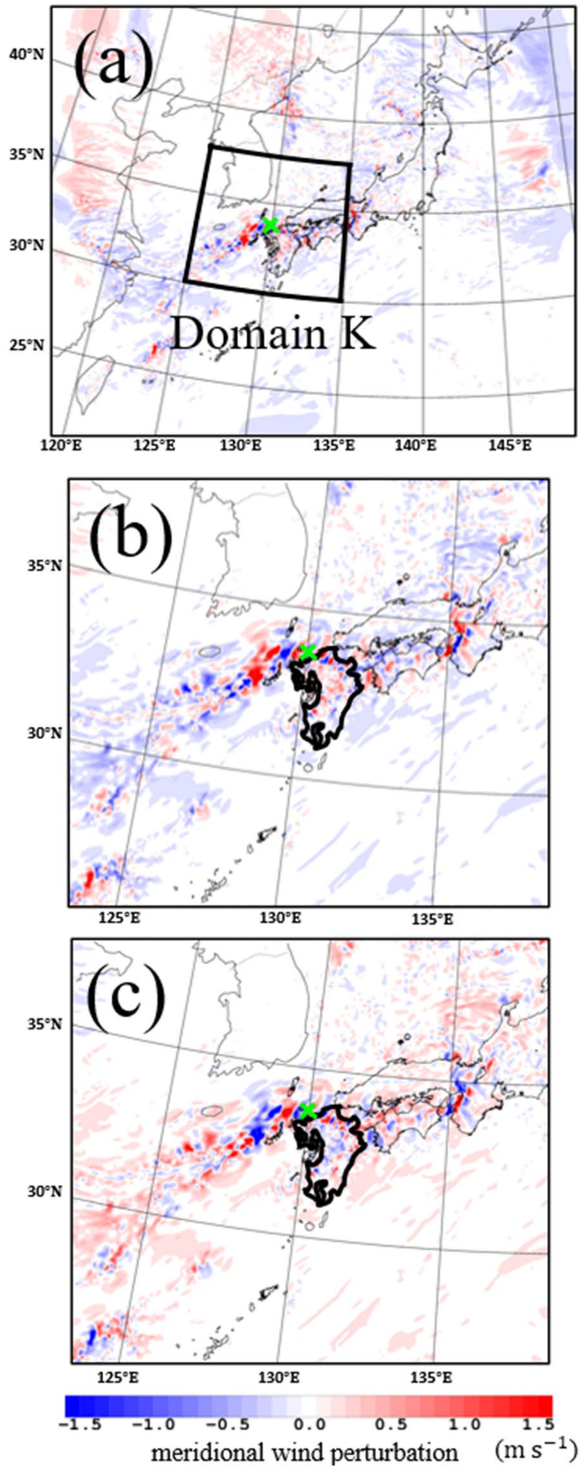

Fig. 2.4. (a) Initial perturbations of meridional wind (m s^{-1}) on the 21st model level (~850 hPa) at 0600 UTC on 13 August 2021. The color scale is shown at the bottom of the figure. The area enclosed by the black line is domain K, used in the calculation of relative nonlinearity (Section 3.1). (b) Enlarged view of Kyushu Island in (a), not the same as domain K. (c) Same as (b), but for the opposite sign for the negative run (see Section 2.3). The green cross indicates the center of domain K.

other as run N. The meaning of P and N is positive and negative, regardless of the sign in the real field of any variables, as in Fig. 2.4. For example, run P gave an initial perturbation field of meridional wind on the 21st model level (~850 hPa; Fig. 2.4b). In run N, the initial perturbation with the opposite sign (Fig. 2.4c) was added to the control's initial field. The perturbations were on the convective scale and mesoscale and had large magnitudes along the stationary front, where the strong rainfall was observed (Fig. 1.1c). In contrast, the perturbations had smaller magnitudes and a larger scale near the lateral boundaries, reflecting the perturbation from the global ensemble prediction system. The perturbation magnitudes were much smaller on the southeastern side of the domain where the subtropical high prevailed (Figs. 2.3b,c).

Regarding to the water vapor initial perturbations, the amount of water vapor exceeding its saturation value was dumped in the perturbed initial conditions (e.g. Sawada and Honda 2021). Although this procedure might collapse the complete opposite direction of the initial perturbations, the bred vectors are characterized by the positive potential temperature perturbation with the positive water vapor perturbation in the saturated background environment to avoid oversaturation (not shown).

Additional pairs of positive and negative perturbation runs were performed to detect the origin of the nonlinearity in the initial field. In these runs, the initial perturbations based on the first bred vector were confined to a 40-km radius centered at 32°N, 127°E (runs pF and nF) and 33°N, 129°E (runs pF' and nF'), where the heavy rainfall was observed in the targeted event on the stationary front. Additionally, the initial perturbations were confined by both above two circles (runs pF" and nF"). The initial perturbations were also confined to a 40-km radius centered at 28°N, 131°E (runs pS and nS) and 32°N, 131°E (runs pS' and nS') on the southern side of the heavy rainfall area on the stationary front.

We also investigated the sensitivity of the perturbed variables at the initial time by modifying runs pF" and nF" through the limiting wind, potential temperature, and water vapor perturbations, and these runs were called pW, nW, pT, nT, pQ, and nQ, respectively. Runs pD and nD investigated the importance of moist physics to the nonlinear signals. These runs were same as runs pF’’ and nF’’ without the convective parameterization and the cloud microphysics in the model runs. Runs P, N, pF’’, and nF’’ based on the second bred vector were conducted for an auxiliary use in Figs. 4.7 and 4.11, thus were not specifically nominated.

Table 2.1: Experiment setting for all runs.

Run name	Perturbation	Perturbed variables	Perturbed area	Model physics
Run C	None	N/A	N/A	All
Run N/P	First BGM	All	Entire model domain	All
Run nF/pF	First BGM	All	40-km circle around 32°N, 127°E.	All
Run nF'/pF'	First BGM	All	40-km circle around 33°N, 129°E.	All
Run nF''/pF''	First BGM	All	40-km circles around 32°N, 127°E and around 33°N, 129°E.	All
Run nS/pS	First BGM	All	40-km circle around 28°N, 131°E.	All
Run nS'/pS'	First BGM	All	40-km circle around 32°N, 131°E.	All
Run nW/pW	First BGM	Wind vector	40-km circles around 32°N, 127°E and around 33°N, 129°E.	All
Run nT/pT	First BGM	Potential temperature	40-km circles around 32°N, 127°E and around 33°N, 129°E.	All
Run nQ/pQ	First BGM	Water vapor mixing ratio	40-km circles around 32°N, 127°E and around 33°N, 129°E.	All
Run nD/pD	First BGM	All	40-km circles around 32°N, 127°E and around 33°N, 129°E.	*

BGM: breeding of growing mode.

(*) Without convective parameterization and cloud microphysics.

Chapter 3. Analysis method

3.1. Evaluation of nonlinearity

The nonlinear signals in the initial perturbation growth were evaluated by relative nonlinearity $\Theta(t)$ (Gilmour et al. 2001),

$$\Theta(t) = \frac{\|\boldsymbol{\delta}^{+}(t) + \boldsymbol{\delta}^{-}(t)\|}{0.5(\|\boldsymbol{\delta}^{+}(t)\| + \|\boldsymbol{\delta}^{-}(t)\|)}, \tag{3.1}$$

where $\|\cdot\|$ denotes an appropriate norm. $\boldsymbol{\delta}^{+}(t)$ and $\boldsymbol{\delta}^{-}(t)$ are the perturbations with each sign at forecast time t; thus, they should initially have the same magnitude and opposite directions, that is, $\boldsymbol{\delta}^{+}(0) = -\boldsymbol{\delta}^{-}(0)$. The relative nonlinearity is zero for perturbation growth in a completely linear system. In a nonlinear system, the relative nonlinearity generally increases to ~1.72 when state vectors $\boldsymbol{\delta}^{+}(t)$ and $\boldsymbol{\delta}^{-}(t)$ have a completely random structure (Hohenegger and Schär 2007b; Appendix A). The maximum relative nonlinearity is 2 when the two perturbations point in the same direction. As the term $\boldsymbol{\delta}^{+}(t) + \boldsymbol{\delta}^{-}(t)$ indicates the degree of nonlinearity between a pair of perturbations, we defined this term as 'nonlinear signal' and analyzed it in this study.

Hohenegger and Schär (2007b) prudently introduced relative nonlinearity to indicate the upper-bound time that a tangential linear model accompanying with the forecast model is valid in an operational forecast system. However, the relative nonlinearity calculated with a single pair of initial perturbations is inadequate for assessing the degree of nonlinearity in a system (Gilmour et al. 2001), even among initial perturbations with greatest growth in the model run. This paper only used this metric to diagnose the similarity of state-vector pattens for a particular pair of initial perturbations. We evaluated how nonlinear the signal is, not how nonlinear the system is. Although the nonlinearity in the system may arise from the product of dependent variables in the governing equations, namely, the nonlinear term, we do not directly treat it as nonlinearity.

We applied relative nonlinearity to the analysis of a pair of perturbed runs in this paper. The relative nonlinearity was computed by a perturbation growth vector composed of three-dimensional zonal and meridional wind, potential temperature, water vapor mixing ratio, and surface pressure as $\boldsymbol{\delta}^{\pm}(t) = \left(\delta u^{\pm}\ \delta v^{\pm}\ \delta\theta^{\pm}\ \delta q^{\pm}\ \delta p_s^{\pm}\right)^{\mathbf{T}}$. We formally used the norm of Eq. (2.1), but the horizontal integration was limited to domain K, fully covering Kyushu Island, Japan (Fig. 2.1a). The size of the domain K was set to diagnose the relative nonlinearity related to the rainband around Kyushu. The size dependency on domain K was small (Fig. 3.1) because the dominant amplitude of perturbations made the main contribution to the relative nonlinearity near the front.

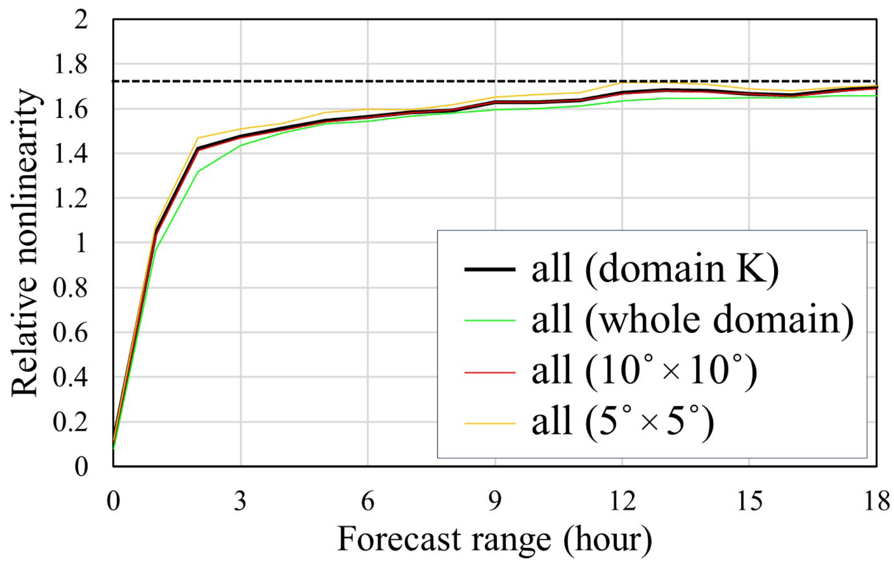

Fig. 3.1. Relative nonlinearity as a function of forecast time (h) between the 16th and 26th model levels. Calculated in (black) domain K (Fig. 2.3a), (green) whole forecast domain, (red) domain within 27.5°N to 37.5°N and 125°E to 135°E, and (yellow) domain within 30°N to 35°N and 127.5°E to 132.5°E.

When the relative nonlinearity was also computed for a single variable, the vector components related to the other variables were replaced with zero. For example, the relative nonlinearity for meridional wind was computed by the perturbation growth vector, $\boldsymbol{\delta}^{\pm}(t) = (0\ \delta v^{\pm}\ 0\ 0\ 0)^{\mathbf{T}}$. In another case, the relative nonlinearity for filtered meridional wind was defined as Eq. (3.1) but with $\boldsymbol{\delta}^{\pm}(t) = \left(0\ \widetilde{\delta v}^{\pm}\ 0\ 0\ 0\right)^{\mathbf{T}}$, where the tilde indicates a filtered variable (Section 3.2).

As explained in Section 2.3, the amount of positive water vapor perturbations could be slightly reduced for the avoidance of over-saturation. This causes a non-zero value of the relative nonlinearity at the initial time. However, we ignored it as its value is about 0.1 or less.

3.2. Spatial filtering

We applied spatial filtering to the initial perturbations and the resulting forecast fields by a two-dimensional fast Fourier transform (FFT). First, the model domain of 1585 × 1305 was extended to a domain of 1600 × 1600 by zero padding out of the model domain. This enlarged perturbation field, with zonal and meridional directions widths of X, Y = 3198 km, $f(x, y)$, can be expanded as

$$f(x,y) = \sum_{|k|\leq K} \sum_{|l|\leq L} f_{kl} e^{-ik\frac{2\pi x}{X}} e^{-il\frac{2\pi y}{Y}}, \tag{3.2}$$

where $K = 1131$ and $L = 1131$ are the wavenumbers (spatial scale at ~3 km) corresponding to the Nyquist frequencies. The low-pass and high-pass filters were designed as the half-amplitude point in weighting coefficient f_{kl} at $k^2 + l^2 = 10^2$ corresponding to the spatial scale at 320 km (see Section 4.2 for the scale selection). The transition band was at wavelengths from 290 to 350 km. The aliasing error was automatically avoided in our analysis, because the perturbations were close to zero owing to Rayleigh damping (Section 2.1) for the same lateral boundary, except for the initial time, in all runs.

To ensure careful treatment in the spatial filtering in our analysis, we applied the Hanning window,

$$W(i) = \frac{1}{2}\left[1 - \cos\left(2\pi \frac{i - 0.5}{N_X}\right)\right], i = 1,2, \dots N_X, \tag{3.3}$$

to perturbations before FFT filtering. Here, i is the grid point number and N_X is the number of grid points in the zonal direction. This window was also applied to the perturbation field in the meridional direction. We did not perform preprocessing for detrending because the perturbations have no domain-scale gradient.

Chapter 4. Results

4.1. Model performance

Initially, we briefly evaluated the performance of JMA's operational model for the target heavy rainfall event comparing the 1-h precipitation rate from run C's 12-h forecast valid at 1800 UTC on 13 August 2021 to the observed precipitation (Fig. 4.1). A line-shaped rainband was observed over the northern part of Kyushu Island, Japan (Fig. 4.1a), with the peak precipitation rate exceeding 50 mm h^{-1}. Run C forecasted this rainband, with a small southwestward bias of about 80 km in the position compared with the observations. Runs P and N also forecasted this rainband, and their forecast difference from run C was large at convective scales.

Related to this rainband, the deep convection line with a width of > 20 km was also reproduced by run C, though the position of the line was slightly biased southwestward (Fig. 4.2). This positional bias did not affect our intended topic to analyze the upscaling process of perturbations from convective scale to mesoscale. Therefore, we confirmed that the model's control run was able to reproduce the rainband and deep convections in the targeted event.

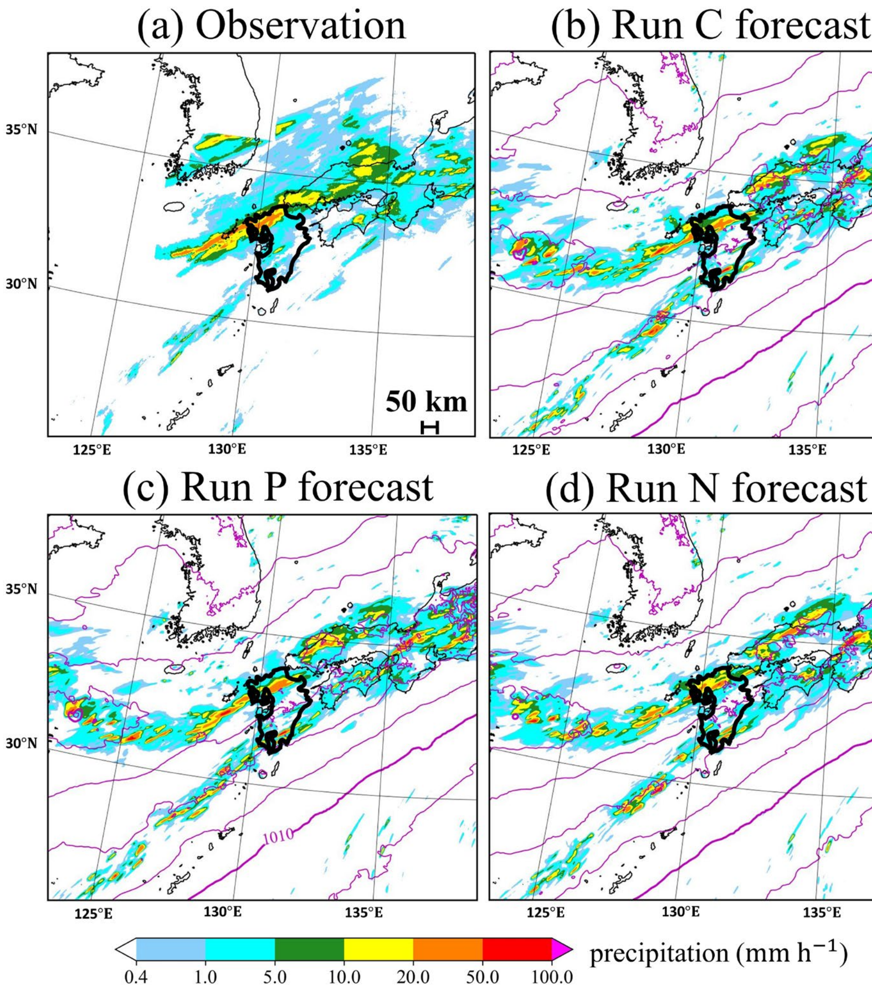

Fig. 4.1. One-hour accumulated precipitation (mm h^{-1}) around Kyushu Island, Japan at 1800 UTC on 13 August 2021 for (a) the R/A observation and (b,c,d) runs C, P, and N at f = 12 h. The color scale is shown at the bottom. In (b,c,d), the mean sea level pressure is superimposed as magenta contours with an interval of 2 hPa. Note that the accuracy of radar observations decreases the further away from the land and no precipitation is observed west of the Korean Peninsula as it is outside the observation range.

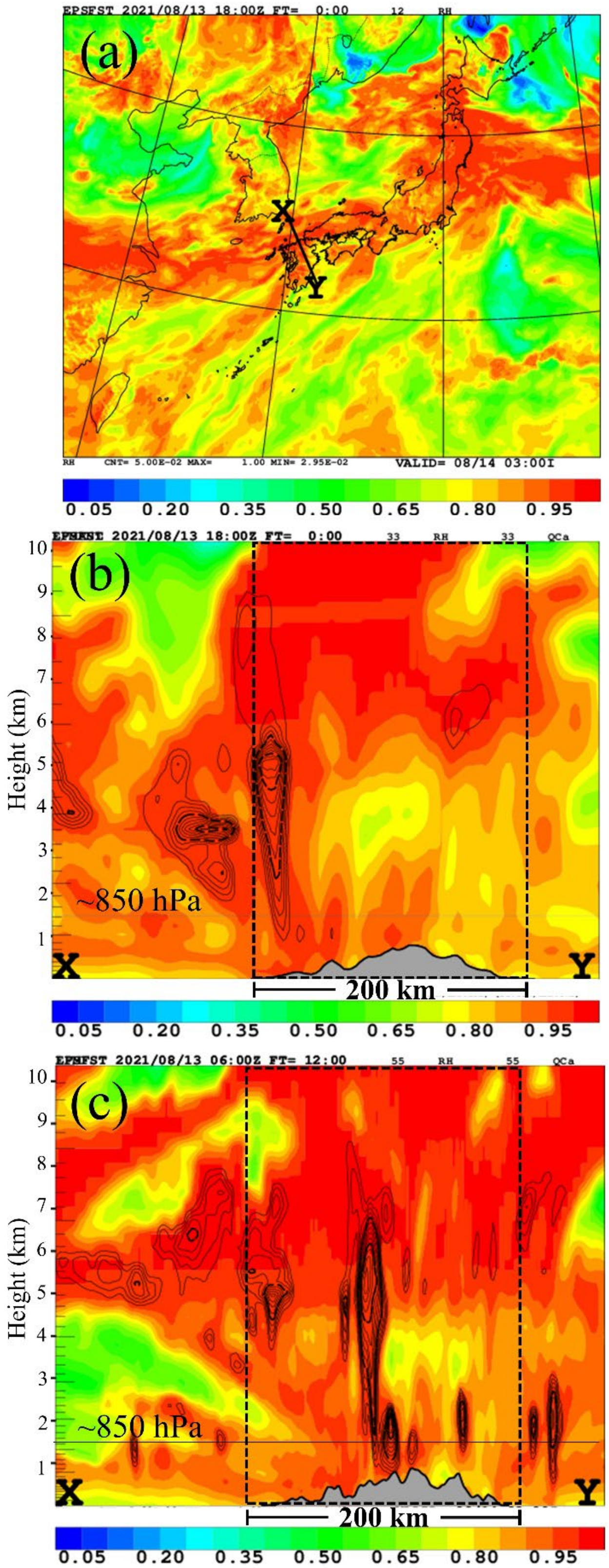

Fig. 4.2. (a) Relative humidity at the 21st model layer (~850 hPa) from the analysis with a 5-km grid spacing at 1800 UTC on 13 August 2021. (b) Vertical cross section of relative humidity along the line segment X to Y in (a). Cloud water is superimposed as black contours with an interval of 0.1 g kg^{-1} in (b) and (c). The outer lines indicate the value of 0.1 g kg^{-1}. The region sandwiched between black dotted lines is Kyushu. (c) Same as (b), but for the run C at f = 12 h.

4.2. Nonlinear perturbation growth

Figure 4.3 shows the spatial distribution of the perturbation of runs P and N for the meridional wind on the 21st model level (~850 hPa) at forecast times of 2 and 12 h (hereafter, f = X h refers to forecast time at X hours). We focus on this level in this study, because this level is the representation level of the lower atmospheric flow near the top of the boundary layer. In particular, moist air flows around this level may determine where MCS occurs in a summer monsoon environment. In both runs, convective-scale perturbation occurred over the rainband, in contrast with the small growth signals over the ocean in the southwest (Figs. 4.3a,c). The convective-scale perturbation between the runs appeared to be random especially at f = 12 h (Figs. 4.3b,d), confirming that the spatial correlation between the perturbations in domain K was about 0.4, indicating randomness[3]. (Hohenegger and Schär 2007a). Runs P and N both developed the same-sign signals for meso-α scale meridional wind perturbation around Kyushu Island: a positive signal over the northern Kyushu area and two negative signals to the northeast and southwest after f = 12 h (white arrows in Figs. 4.3b,d). This same sign in the perturbation field was a signal of nonlinear perturbation growth in the environment where the midlatitude MCS was observed.

Figure 4.4 shows the nonlinear signals from runs P and N for the meridional wind on the 21st model level at f = 2 and 12 h. The nonlinear signal was found along the front at f = 2 h., and was developed around the Kyushu island at f = 12 h, especially along the front same as Figs 4.3b,d.

---

[3] According to Hohenegger and Schär (2007a), if the perturbations are calculated by the field with smaller variance than run C, the random structure corresponds to 0.0 of the spatial correlation between perturbations. However, the perturbations were calculated from run C, which has almost same variance with runs P and N, the random structure of them corresponds to the spatial correlation value of 0.5.

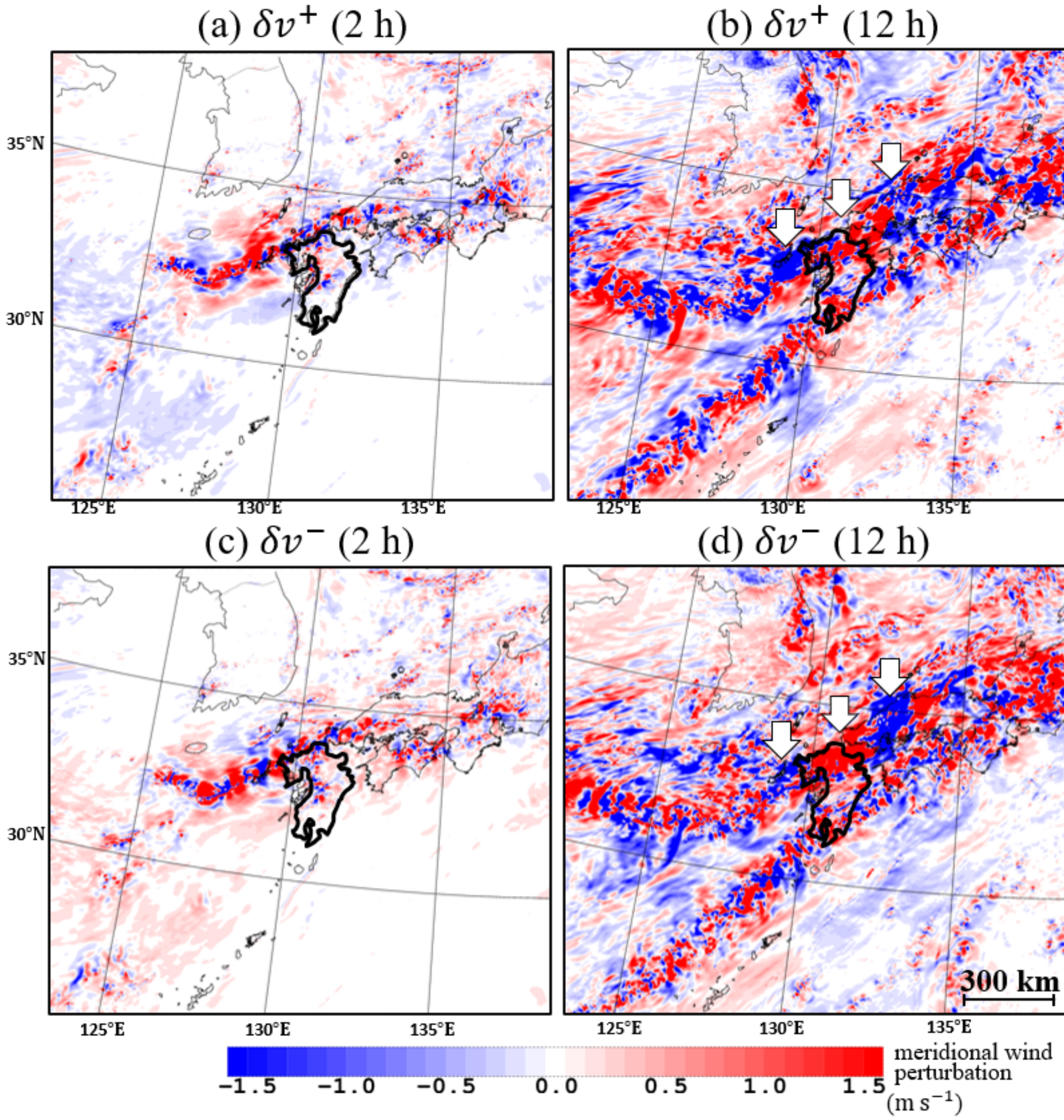

Fig. 4.3. (a,b) Meridional wind perturbation (m s^{-1}) on the 21st model level (~850 hPa) in run P at (a) f = 2 h and (b) f = 12 h. White open arrows in (b) help to explain the nonlinearity in the text. (c,d) Same as (a,b), but for run N.

The relative nonlinearity in runs P and N (Fig. 4.5) increased considerably in the first 2 h of the forecast, corresponding to rapid convective-scale perturbation growth. Thereafter, the relative nonlinearity increased gradually toward the randomness level at ~1.72, consistent with Hohenegger and Schär (2007b). For example, the relative nonlinearity evaluated with selected

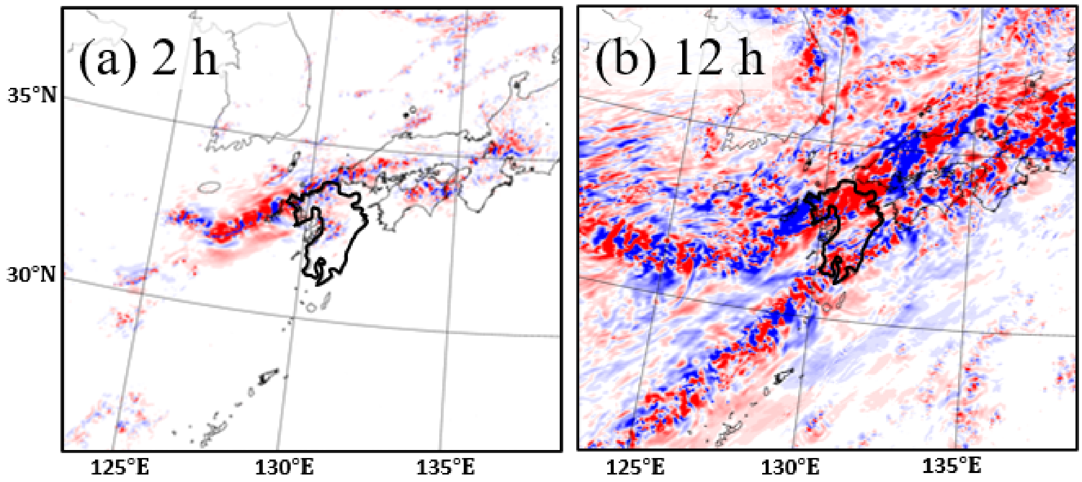

Fig. 4.4. Nonlinear signals for meridional wind perturbation (m s^{-1}) on the 21st model level (~850 hPa) from runs P and N at (a) f = 2 h and (b) f = 12 h.

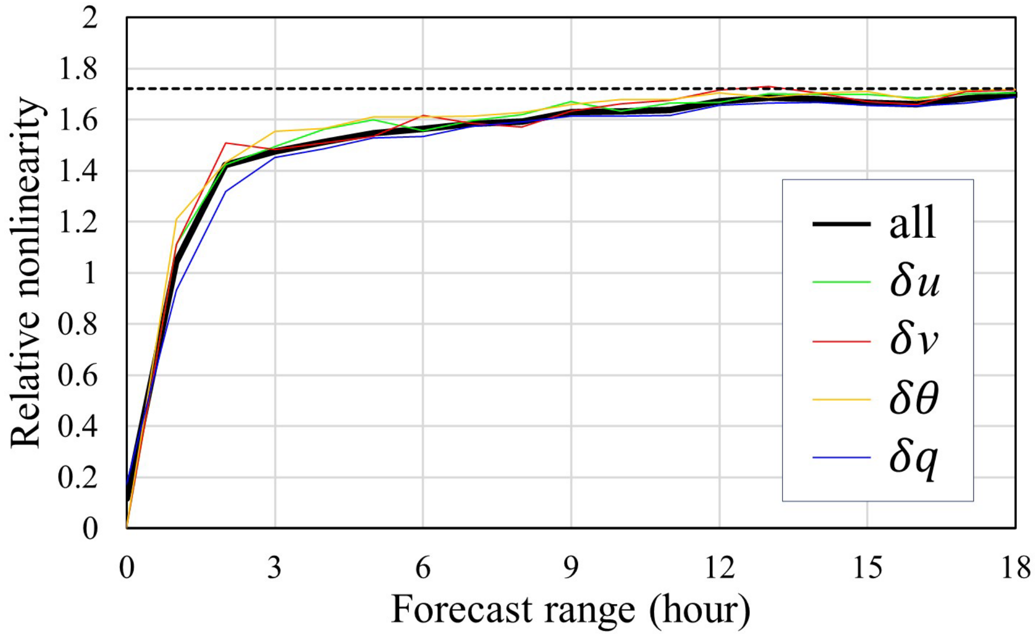

Fig. 4.5. Relative nonlinearity for all variables and each variable calculated between the 16th and 26th model levels (approximately between 900 and 2200 m). The dotted horizontal line denotes the relative nonlinearity value of ~1.72.

state-vector components related to meridional wind was close to 1.72 at f = 11 to 13 h, corresponding to a random structure between a pair of runs around Kyushu Island (Figs. 4.4b).

To extract the meso-α scale structure from the perturbation fields, we applied a spatial low-pass filter with a cutoff wavelength of 320 km to all perturbation fields for runs P and N. The reason for the selection of the cut off wavelength will be explained later in this section. Figure 4.6 shows the low-pass filtered nonlinear signals for zonal and meridional wind, potential temperature and water vapor. The large signals were found around the line-shaped rainband near the Kyushu area. The nonlinear signal of the meridional wind perturbation pair has negative sign over the western sea around Kyushu, positive sign over Kyushu, and negative sign over the east of Kyushu. Other variables also had the nonlinear signals. For example, the potential temperature was positive signal over Kyushu. The zonal wind and water vapor also had nonlinear signals around Kyushu, but its amplitude is smaller than that of meridional wind, indicating slightly smaller relative nonlinearity than the meridional wind perturbations.

Temporal evolution of nonlinear signals enabled us to understand how those signals emerged and developed (Fig. 4.7). At the initial time (Fig. 4.7a), we imposed an absolutely antisymmetric perturbation between runs P and N indicating the no nonlinear signals. The perturbation magnitudes were small, and the initial perturbation field had a predominant convective-scale component (Fig. 2.4). In the first 3 h (Figs. 4.7b–d), the nonlinear signal increased around the Tsushima Strait between the Korean Peninsula and Kyushu Island only in run P (white arrow in Figs. 4.7c,d), showing the upscaling of perturbations from the convective to meso-α scales on the line-shaped rainband. However, this nonlinear growth almost stopped at

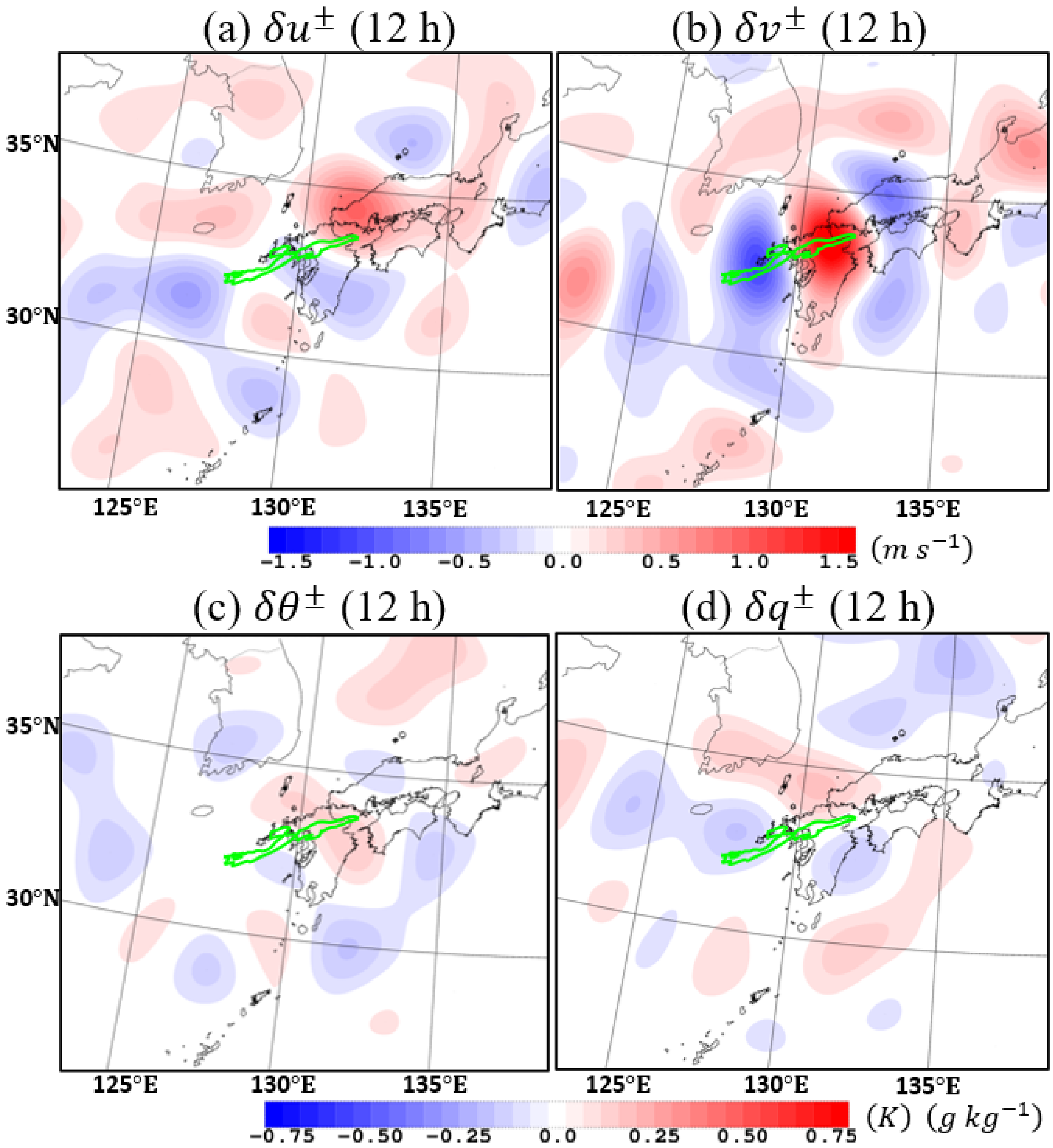

Fig. 4.6. Low-pass-filtered nonlinear signals of (a) zonal wind (m s^{-1}), (b) meridional wind (m s^{-1}), (c) potential temperature (K), and (d) water vapor (g kg^{-1}) on the 21st model level at f = 12 h. The green line is the contour line for precipitation forecasted by run C of 10 mm h^{-1}, including areas exceeding 50 mm h^{-1}.

f = 4 h (Fig. 4.7e). A sequence of positive/negative patterns emerged and moved eastward until f = 9 h (Fig. 4.7j). At f = 10 h, these patterns were enhanced on the line-shaped rainband (white allows in Fig. 4.7k). These nonlinear signals were stagnant by f = 12 h, and the their magnitudes were increased (Figs. 4.7k–m), as seen in the unfiltered perturbation fields (Figs. 4.3b,d). This nonlinear signal was also confirmed in another set of runs P and N initialized by the second bred vector (Fig. 4.7n).

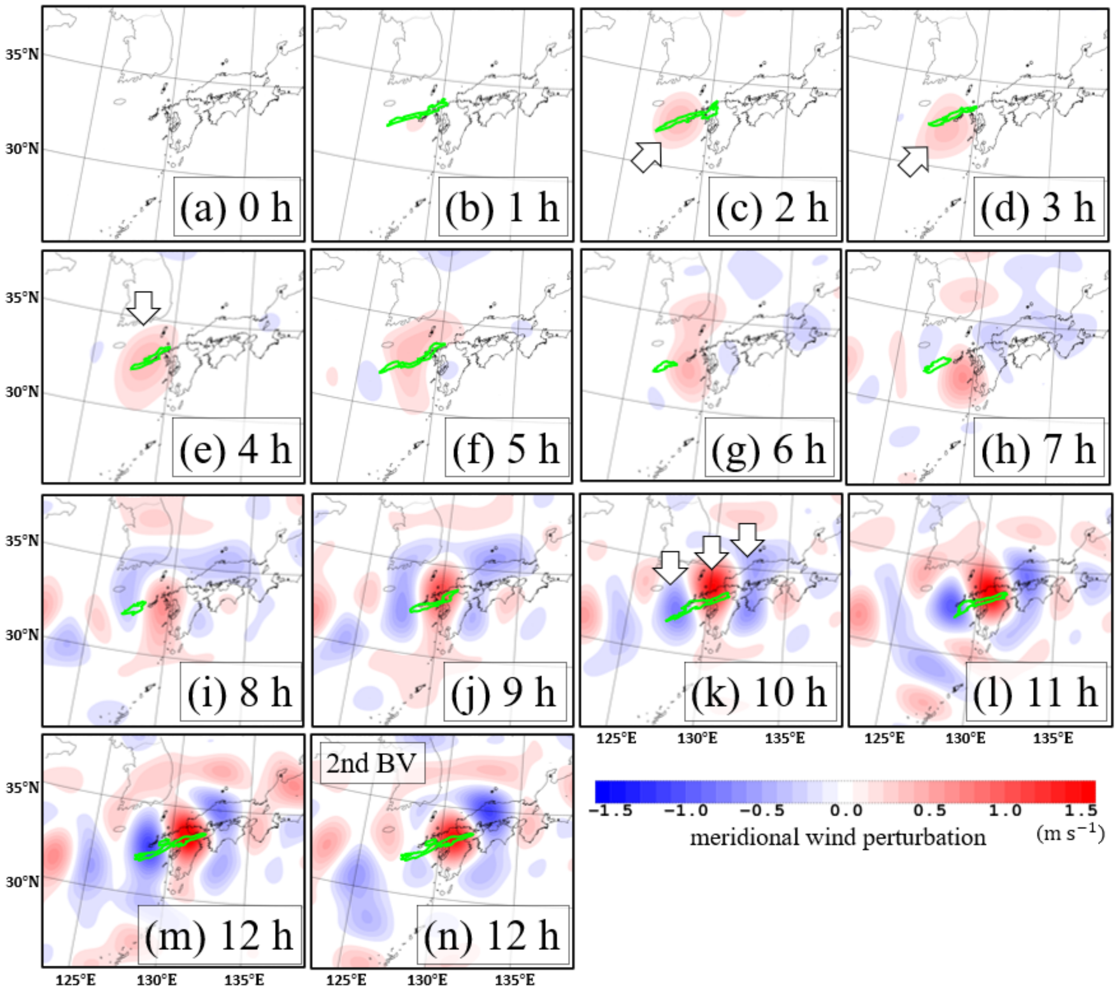

Fig. 4.7 Low-pass-filtered meridional wind nonlinear signal (m s^{-1}) on the 21st model level from (a)−(m) f = 0 to 12 h from runs P and N. (n) Same as (m), but based on the second bred vector. The white arrows in (c,d,e,k) are to help the explanations in the text. The green line is the contour line for precipitation forecasted by run C of 10 mm h^{-1}, including areas exceeding 50 mm h^{-1}.

The relative nonlinearity evaluated with selected components of filtered meridional wind perturbations for a pair of runs P and N is shown in Fig. 4.8. The relative nonlinearity from high-pass-filtered meridional wind perturbations grew rapidly in the first 2 h, regardless of the cutoff wavelength between 20 and 80 km (Fig. 4.8a). These results were similar to those from the perturbations without a spatial filter (Fig. 4.5). This is because the amplitude of the perturbations was dominant at the convective scale reflecting the relative nonlinearity of the convective scales The relative nonlinearity with low-pass-filtered meridional wind perturbation also increased rapidly in the first 2 h (Fig. 4.8b). This rapid growth corresponded to the nonlinear upscaling seen in Figs. 4.7c,d. In contrast, the relative nonlinearity based on the low-pass-filtered perturbations of runs P and N was characterized by a gradual increase during f = 4 to 8 h and was almost saturated at the randomness level of ~1.72 around f = 10 h, reflected by the sign of a sequence-like nonlinear signal and its gradual increase (Figs. 4.7d–j). After f = 9 h, the relative nonlinearity with low-pass-filtered perturbations with a cutoff wavelength of 320 km exceeded 1.72, consistent with the intensive nonlinear signal (Figs. 4.7k–m).

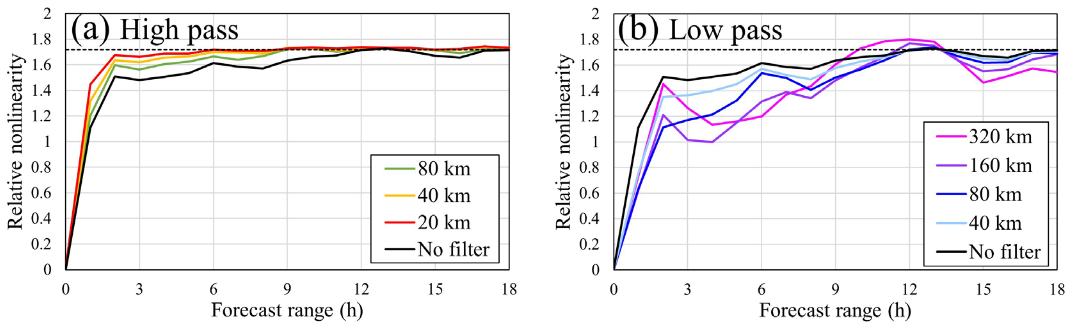

Fig. 4.8 Relative nonlinearity for (a) high-pass and (b) low-pass-filtered meridional wind perturbation calculated between the 16th and 26th model levels. The dotted horizontal line denotes the relative nonlinearity value of ~1.72.

The contrast between low-pass and high-pass results (Fig. 4.8) suggested that the nonlinear signals of the perturbation were upscaled from the convective scale (Fig. 4.7c), which may be related to the meso-α scale structure with the same-sign perturbations near the rainband at f = 10 h in runs P and N (Fig. 4.3b,d7k). The relative nonlinearity was high at the cutoff wavelength of 320 km (Fig. 4.8b). This is the reason why we selected 320 km as the cutoff wavelength for the spatial filtering.

4.3. Origin of the nonlinear signals

In the previous subsection, we found nonlinear signals with a high relative nonlinearity on a scale of more than 320 km related to the upscaling from convective scales around the active convection area. However, it is difficult to investigate the origin of nonlinear signals in widespread, complex, multiscale MCSs. We therefore examined the initial perturbation sensitivity to the nonlinear signals around the line-shaped rainband in runs P and N (Fig. 4.7) by performing additional runs with an initial patch perturbation (Table 2.1). The origin of the upscaling process can be identified by the contribution of the patch perturbation to the nonlinear signals in runs P and N. The sensitivity of the perturbed variables and moist physics to the nonlinear signals and the upscaling process was also investigated.

4.3.1. Sensitivity to the initial perturbations

In the additional runs, we trimmed the initial perturbations based on bred vectors within a radius of 40 km from a point at the stationary front or its southern side (Figs. 4.9a,c,e,g,i). We chose 40 km as the perturbation patch size because it exceeds the smallest scale of a convection that the forecast model can represent sufficiently. The patch size sensitivity to nonlinear signals will be reported elsewhere.

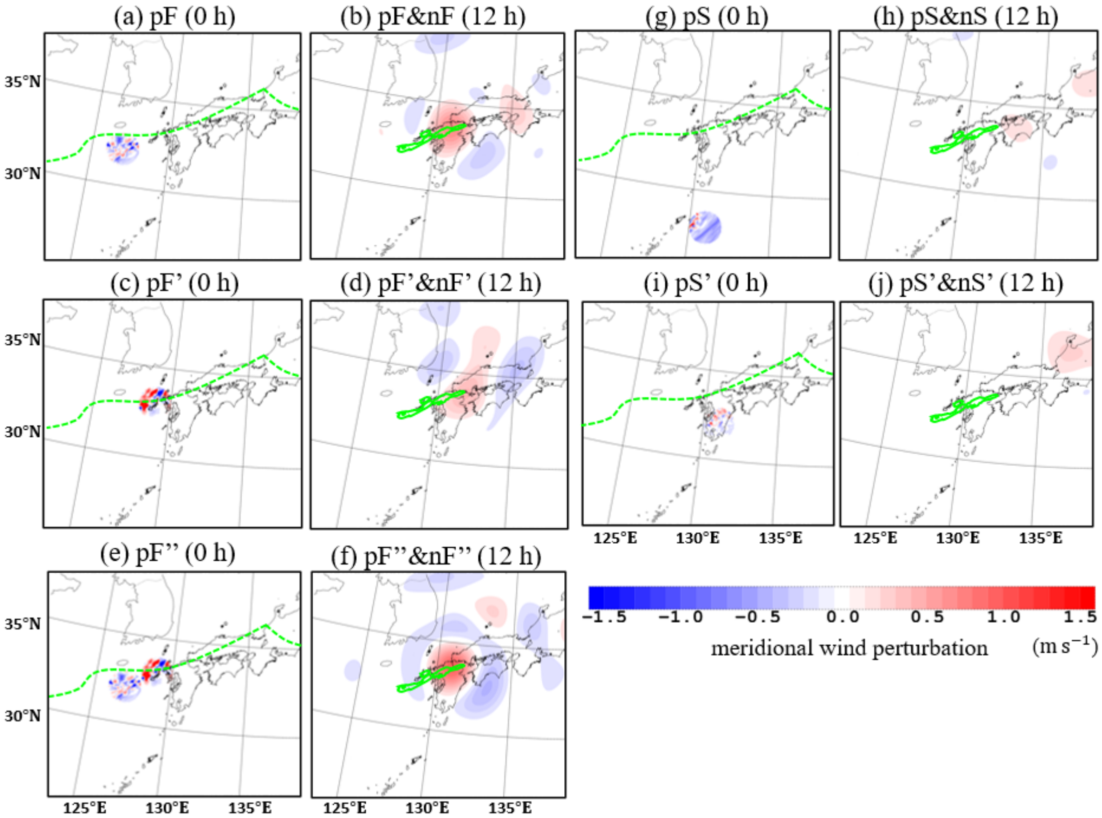

Fig. 4.9 (a,c,e,g,i) Meridional wind perturbation (m s^{-1}) on the 21st model level at the initial time for runs (a) pF, (c) pF', (e) pF'', (g) pS, and (i) pS'. (b,d,f,h,j) Nonlinear signals for meridional wind perturbation (m s^{-1}) on the 21st model level with low-pass spatial filtering with a cutoff wavelength of 320 km at f = 12 h for runs (b) pF and nF, (d) pF' and nF', (f) pF'' and nF'', (h) pS and nS, and (j) pS' and nS'. The green broken line at f = 0 h shows the stationary front in the surface weather chart (Fig. 1.1). The green line at f = 12 h is the contour line for precipitation forecasted by run C of 10 mm h^{-1}, including areas exceeding 50 mm h^{-1}.

Runs pF and nF showed the nonlinear signals over Kyushu and the areas on each side (Fig. 4.9b), but the phases of them were slightly different from those of runs P and N. Runs pF' and nF', in which the perturbation was introduced near the front, also showed similar nonlinear signals, although the signals were located in the downstream region of the rainband (Fig. 4.9d). Runs pF" and nF", in which double patches were imposed as the initial perturbations, showed the positive sign over northern Kyushu Island and negative signs over the areas on each side (Fig. 4.9f) better than any other pair of runs. These runs indicated that the nonlinear signals observed at f = 12 h originated from the initial perturbations in the upstream region of the line-shaped rainband on the stationary front where the convection was active. The perturbation out from the stationary front was ineffective in producing the nonlinear signals around Kyushu; runs pS and nS and runs pS' and nS', in which the southern regions of the stationary front were initially perturbed, did not generate strong nonlinear signals (Figs. 4.9h,j).

Figure 4.10 shows the relative nonlinearity of the low-pass-filtered meridional wind perturbations for additional experiments. Runs pF" and nF" showed that the relative nonlinearity rapidly increased in the first 2 h, slightly decreased, and increased again after 5 h, similar to the features of runs P and N. Runs pS, nS, pS' and nS' did not reproduce this rapid increase in the relative nonlinearity. The second peak in runs pF" and nF" occurred at f = 11 h, almost at the same timing as that in runs P and N (around f = 12 h). The time evolution of the relative nonlinearity from runs pF" and nF" was closest to that from runs P and N.

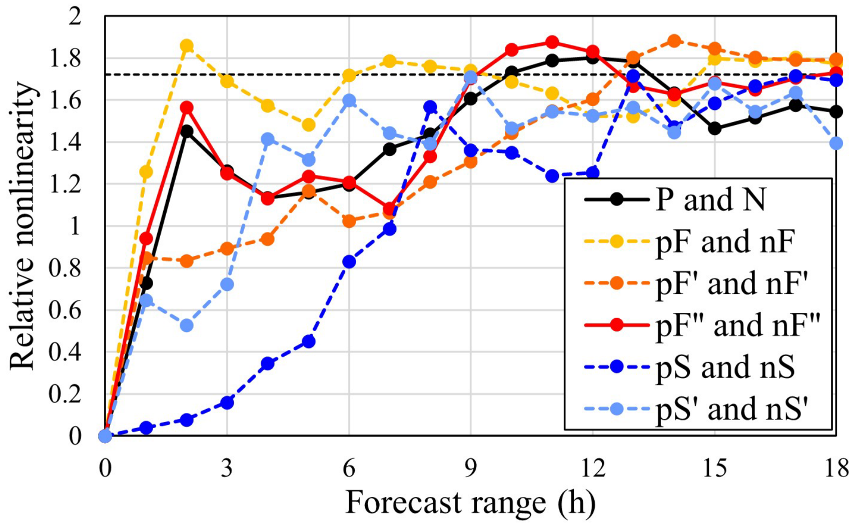

Fig. 4.10 Relative nonlinearity as a function of forecast time (h) for low-pass-filtered meridional wind perturbations calculated between the 16th and 26th model levels for pairs of runs (black) P and N, (yellow) pF and nF, (orange) pF' and nF', (red) pF'' and nF'', (blue) pS and nS, and (skyblue) pS' and nS'. The dotted horizontal line denotes the relative nonlinearity value of ~1.72.

We also confirmed the similarity of the nonlinear signals from runs pF'' and nF'' to runs P and N from the time evolution of the horizontal distribution (Fig. 4.11), that is, the upscaling signal at *f* = 2 h (Fig. 4.11c), the gradual increase of the nonlinear signal at *f* = 4 to 9 h (Figs. 4.11e–j), and the dominant nonlinear signal after *f* = 10 h (Figs. 4.11k–m). This nonlinear signal was also seen in additional runs pF'' and nF'', initialized by the second bred vector (Fig. 4.11n). Considering that runs pF'' and nF'' provided a similar nonlinear signal to runs P and N, and not to other pairs, we explored the origin of the nonlinear signals at the stationary fronts with runs pF” and nF”.

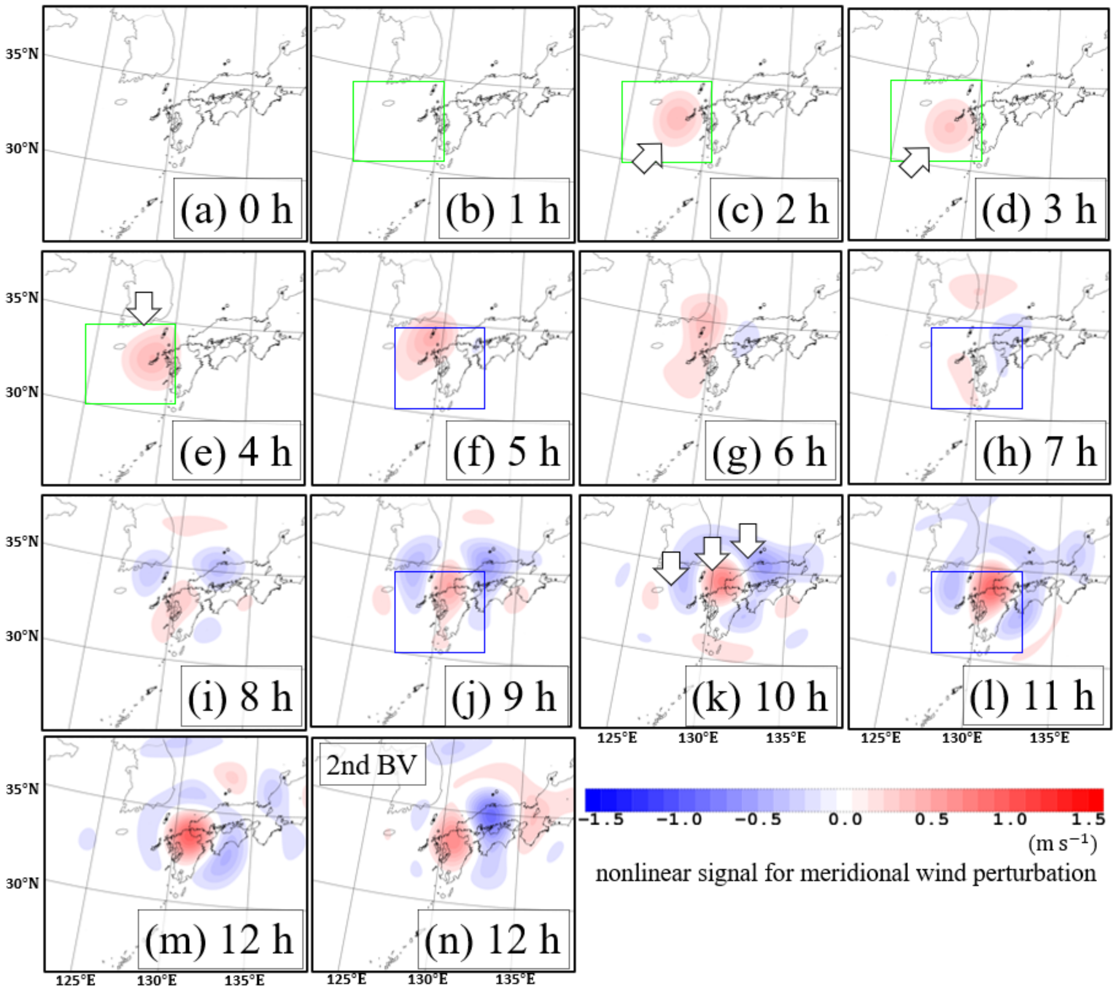

Fig. 4.11 Same as Fig. 4.6, but for runs pF” and nF”. Green boxes show the close-up region in Figs. 4.12. Blue boxes show the close-up region in Figs. 4.13.

4.3.2. Origin of the upscaling process

We analyzed the results for runs pF” and nF” by zooming into the region around the origin of the nonlinear signals to investigate the upscaling process from the convective scale to the meso-α scale. We restored the perturbation fields with no spatial filtering to observe all scales resolved in the model. Figure 4.12 shows the time evolution of the meridional wind perturbation around the initially perturbed region in runs pF'' and nF''. The opposite sign patterns, positive in run pF'' and negative in run nF'' (green arrows in Fig. 4.12), moved eastward and expanded with time.

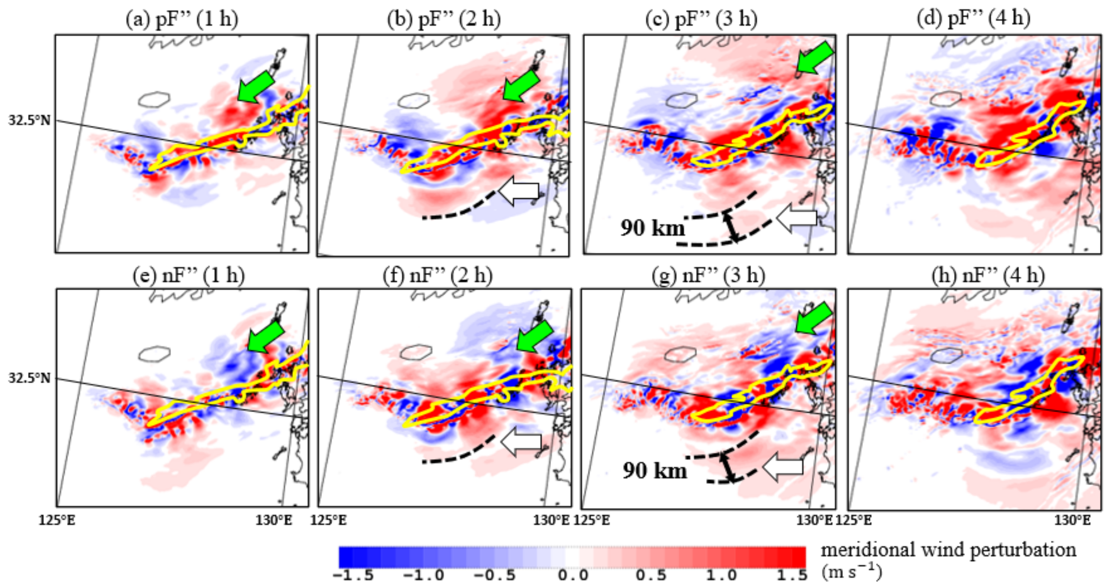

Fig. 4.12 Meridional wind perturbation (m s^{-1}) on the 21st model level at $f = 1$ to 4 h in run pF'' (a–d) and nF'' (e–h). The green and white arrows are to help the explanations in the text. The black broken lines in (b and f) shows the tip of the positive values at $f = 2$ h. The black broken lines in (c and g) show the tips at $f = 2$ and 3 h. The yellow line shows the contour line for precipitation forecasted by run C of 10 mm h^{-1}, including areas exceeding 50 mm h^{-1}.

The southeastern tip of the positive signal moved ~ 90 km from $f = 2$ to 3 h in runs pF'' and nF'' (Figs. 4.12b,c,f,g), indicating that the propagation speed was about 90 km h^{-1}. We estimated the propagation speed of a gravity wave following Selz and Craig (2015). The hydrostatic nonrotating regime yielded the gravity wave speed as the Brunt–Väisälä frequency divided by the vertical wavenumber (Gill 1982). Because the vertical wavenumber was 1 at the tropospheric depth (15 km; not shown) and the Brunt–Väisälä frequency was 0.01 s^{-1} at f = 2 h in domain K, the gravity wave speed was 86 km h^{-1}, suggesting that perturbations were propagated outwards by the gravity wave. These results implied that the gravity waves excited in convective areas were a source of upscaling to the nonlinear perturbation patterns.

The same-sign patterns, positive in both runs, moved eastward after f = 1 h (white arrows in Figs. 4.11a-c,e-g). This pattern corresponded to the nonlinear signal on the meso-α scale (Fig. 4.11c) and the first increase in the relative nonlinearity at f = 2 h (Fig. 4.10). This nonlinear signal dissipated after f = 2 h, and instead, the opposite-sign perturbations prevailed, corresponding to an intermittent decrease in the relative nonlinearity by f = 4 h (Fig. 4.10). After then, the same positive-sign perturbation (white arrows in Fig. 4.13) was westward of the opposite-sign perturbations after f = 5 h. The same negative-sign perturbation was also found after f = 9 h. These nonlinear signals expanded from southwest to northeast at f = 11 h. The dominance of these nonlinear signals contributed to the second gradual increase in the relative nonlinearity by f = 11 h (Fig. 4.10). A possible key process in the expansion of these nonlinear signals from

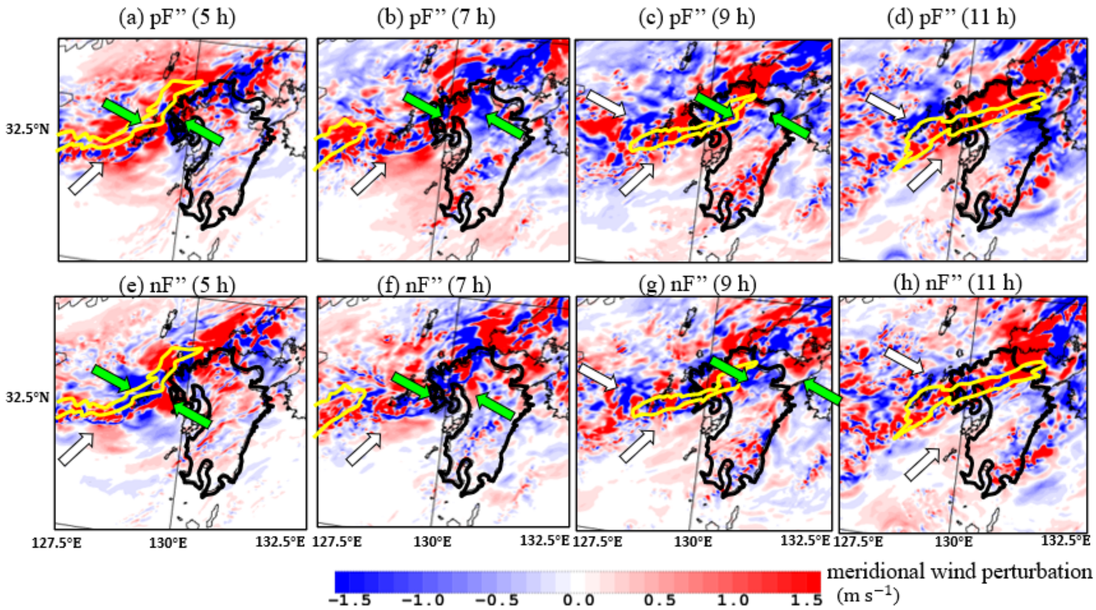

Fig. 4.13 Same as Fig. 4.12, but at f = 5, 7, 9, and 11 h.

the convective area seemed to be the gravity wave propagation in the initial few hours and subsequently the vortex dynamics under a strong shear zone on the stationary front. The vortex dynamics are beyond the scope this paper, and thus we will discuss them elsewhere.

Figure 4.14 shows the power spectra of meridional wind perturbation in run pF'' (Fig. 4.14a) and the ratio of the meridional wind perturbation power spectra for the sum of the perturbations in runs pF'' and nF'' and the double-amplitude perturbation in run pF'' (Fig. 4.14b). Because this sum was the numerator in Eq. (3.1), its non-zero value was the nonlinear component

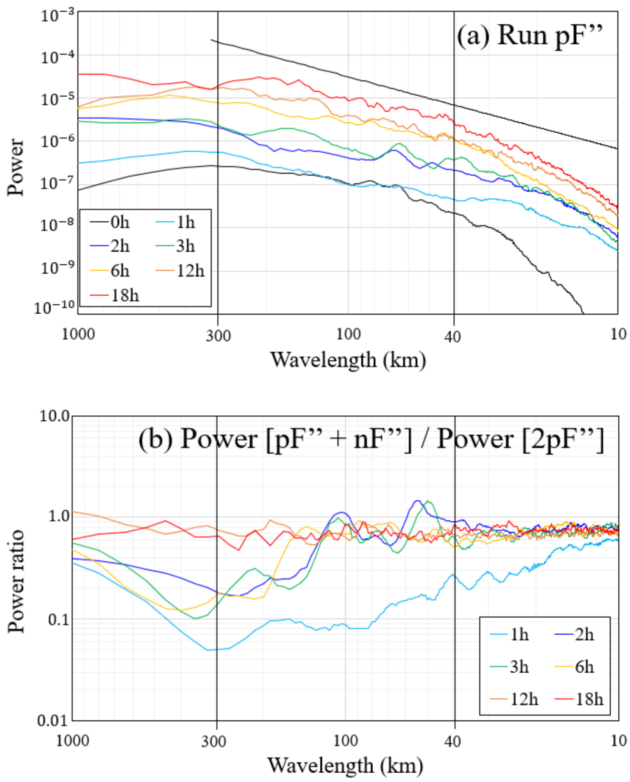

Fig. 4.14 Power spectra of meridional wind perturbation in (a) run pF'' and (b) ratio of between the power spectra of sum of runs pF'' and nF'' and of run pF'' with double amplitude at f = (black) 0, (skyblue) 1, (purple) 2, (green) 3, (yellow) 6, (orange) 12, and (red) 18 h. Black line denotes the −5/3 power law as a reference.

represented by the perturbations in runs pF” and nF”. A ratio value of 1 means that the amplitude of the nonlinear signal is equivalent to twice the amplitude of run pF”.

The perturbation growth of run pF” was significant on a horizontal scale smaller than 40 km during the first 1 h (Fig. 4.14a), indicating the rapid convective-scale perturbation growth. The perturbation on a scale larger than 200 km grew at the same time, showing the larger-scale perturbations were related to the gravity wave propagation. The power ratio also increased rapidly on a scale smaller than 40 km during the first 1 h (Fig. 4.14b). After 1 h, perturbation growth occurred at all scales (Fig. 4.14a). The power ratio increased greatly at all scales until 2 h (Fig. 4.14b). The meso-scale nonlinear signal on a scale larger than 100 km fluctuated after $f = 2$ h, whereas the nonlinear signals on a scale smaller than 100 km attained the saturated value of 0.7–0.8 (Fig. 4.14b). The peak power ratios at $f = 2$ and 3 h, corresponding to a 100 km wavelength, reflected the nonlinear signals in Figs. 4.11b,c,f,g. The power ratio eventually reached the saturated value of 0.7–0.8 at $f = 12$ h on a scale smaller than 300 km, which reflected the strengthening of the nonlinear signals at the meso-α scale (Figs. 4.11k–m). The power spectrum diagnosis for the sum of runs pF” and nF” indicated a clear upscaling of the nonlinear signals simulated in our experiment.

4.3.3. Sensitivities of variables and moist physics

Additional experiments with trimmed perturbations same as pF” and nF” but restricted further to wind, temperature, or water vapor (Fig. 4.15) revealed a contribution comparable to the results above. The low-pass-filtered nonlinear signals for meridional wind perturbation showed that runs with temperature and water vapor perturbation (Figs. 4.15b,c) corresponded to runs pF” and nF” (Fig. 4.11m). The relative nonlinearities from runs pT and nT and runs pQ and nQ increased rapidly by $f = 2$ h (Fig. 4.16), which indicated that the initial perturbations in the potential temperature or water vapor may contribute to the rapid upscaling related to moist convection. In contrast, the runs with wind perturbation less showed nonlinear signals at $f = 12$ h (Fig. 4.15a). However, the relative nonlinearity in runs pW and nW reached its peak in the later stage at $f = 14$ h (Fig. 4.15). Therefore, wind contributed as much as temperature and water vapor to the nonlinear signals on the meso-α scale.

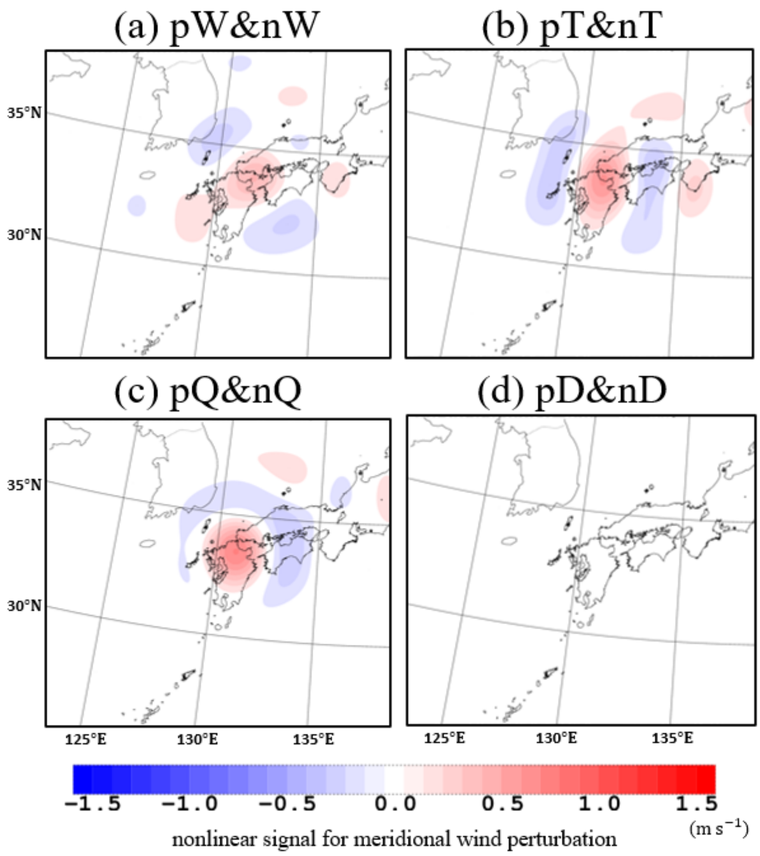

Fig. 4.15 Low-pass-filtered meridional wind perturbation (m s^{-1}) on the 21st model level at $f = 12$ h for pairs of runs (a) pW and nW, (b) pT and nT, (c) pQ and nQ, and (d) pD and nD.

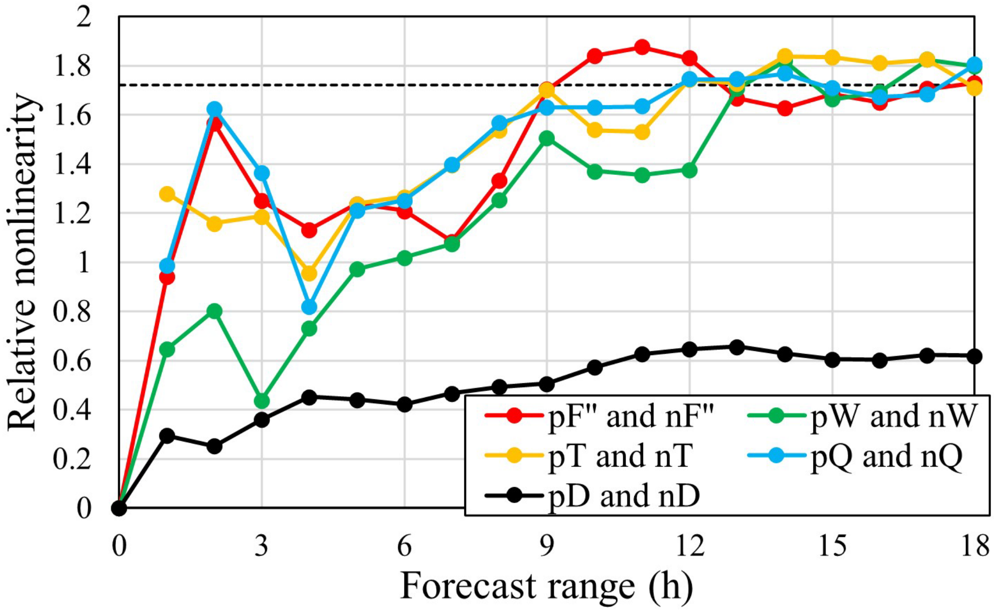

Fig. 4.16 Relative nonlinearity as a function of forecast time (h) for low-pass filtered meridional wind perturbations calculated between the 16th and 26th model levels for pairs of runs (red) pF'' and nF'', (green) pW and nW, (yellow) pT and nT, (skyblue) pQ and nQ, and (black) pD and nD.

Finally, we performed runs pD and nD without the convective parameterization and the cloud microphysics during the model integrations. The signal at f = 12h was almost linear and its amplitude was small compared with the other runs (Fig. 4.15d). A slight upscaling process was detected in the beginning of the forecast time but was likely independent of the convective activities (not shown). The relative nonlinearity remained smaller than in the other run pairs (Fig. 4.16). This supported the idea that the moist physics in the forecasting model was essential for generating nonlinear signals in the convective area.

Chapter 5. Summary

We investigated initial perturbation growth using high-resolution model forecasts of a midlatitude MCS that brought torrential rainfall in western Japan on 13 August 2021 to reveal the nonlinear signals in the forecast. First, we confirmed that the forecast perturbation had the same-signed meso-α scale nonlinear signals that expanded from the center of the rainband. The relative nonlinearity was high after a few forecast hours. The sensitivity of this nonlinear response on the meso-α scale was investigated in additional experiments. The experiments revealed that the nonlinear signals originated in the upstream region of the line-shaped rainband in the initial field. The gravity waves emitted from the rainbands expanded the nonlinear signals from the convective area. In particular, the nonlinear signals on the meso-α scale did not appear from the experiment without the moist physics. These results indicated the importance of gravity waves through moist convections for the nonlinear meso-α scale perturbation patterns in a few hours from the initial forecast time.

This study showed the generation of nonlinear signals near a horizonal shear zone on the stationary front, as identified by the relative nonlinearity. The almost-saturated environment that we targeted in this study made the nonlinear response sensitive to when and where moist convective cells built up. A moisture or low-pressure perturbation may have triggered or suppressed convective cells at those locations. Regardless of the signal sign, this possibly resulted in a different density-surface uplifting in the convective timescales compared with the control run. Although runs pD and nD demonstrated that moist physics was essential for the nonlinear signals, the generation process of the nonlinear perturbation pattern in the convective areas remained unclear and requires further research.

A pair of runs with opposite-sign initial perturbations showed that the nonlinear signals were generated in an almost-saturated environment on the horizontal shear zone. Although this study only focused on the single MCS case in western Japan, the knowledge that we obtained could be applied to other cases in which an environment appears repeatedly in an Asian summer monsoonal season. The nonlinear response could also be detected in moving disturbances such as squall lines and supercells associated with baroclinic waves, because the convective area is almost saturated in the horizontal shear zone. However, the perturbation changes should depend on the advection in the moving disturbances, which is beyond the scope of this study. In contrast to MCSs, it is expected that scattered thunderstorms would not show a nonlinear response on the meso-α scale because the convection is disorganized and the horizontal shear is indistinct. In future work, our findings could be applied to other convective systems.

Chapter 6. General conclusion

We studied the nonlinear initial perturbation growth in an MCS by using a high-resolution forecasting model and newly found the rapid nonlinear perturbation growth at the mesoscale as well as the convective scale (Hohenegger and Schär 2007b). Previous studies showed the linear perturbation growth for severe weather events with the mesoscale models being the horizontal grid spacing of 10 − 100 km, which did not explicitly resolve convective activity (e.g. Ancel and Mass 2006; Lang et al. 2012; Demirdjian et al. 2020). Therefore, the high-resolution forecast enabled us to reveal the novel perspective of the perturbation growth at mesoscale.

There have been many studies related to the perturbation growth in severe weather events in the U.S., where the MCSs were frequently observed on the continent (e.g. Johnson and Wang 2016; Minamide et al. 2020; Schwartz et al. 2022). However, less researches for initial perturbation growth in mesoscale models has been conducted in the environment with the abundant water vapor surrounded by the ocean, like Japan, despite that some studies focused on precipitation forecast performance (e.g. Oizumi et al. 2020; Kato 2020; Duc et al. 2021). In this regard, this study firstly revealed the perturbation growth in the environment with multiscale phenomena that included heavy precipitation along with the persistent line-shaped rainband under the summertime Asian monsoon system.

This study shows that the linearity of a pair of perturbations in a high-resolution forecast is lost during the first few hours in the active convection areas. The validity of tangential linear approximation is a key of how to improve the operational forecasting system, because many weather centers have adopted the four-dimensional variational data assimilation (4DVar) to generate initial conditions. With the recent progress of computer technology, many operational weather centers have increased the model resolution for regional models (e.g. Milan et al. 2020; Kusabiraki et al. 2021) and global models (e.g. Haiden et al. 2023; Yonehara et al. 2023). These systems will face the collapse of a tangential linear approximation toward a more accurate initial condition with higher resolution models on active convective areas which are so important for the forecast of severe weather events. Our results will contribute to the development of initial conditions by providing the insights of nonlinearity in MCSs.

Acknowledgments

I would like to express my gratitude thanks to Prof. Masaru Inatsu, who is the supervisor of my doctoral course, for supporting this study and suggesting valuable comments and discussions. I also deeply thank the other committee members of this dissertation: Prof. Shoshiro Minobe, Dr. Yoshinori Sasaki, Dr. Yousuke Sato, and Prof. Tetsuya Takemi. I would like to thank Dr. Hiroaki Miura and Dr. Takuya Kawabata for giving me many suggestions for my work. I thank the laboratory members for giving me great time. This work was supported by JSPS KAKENHI Grant Number 23K03498; the Advanced Studies of Climate Change Projection (SENTAN) Grant Number JPMXD0722680734 of the Ministry of Education, Culture, Sports, Science, and Technology, Japan; and by Research Field of Hokkaido Weather Forecast and Technology Development (endowed by Hokkaido Weather Technology Center Co., Ltd.). Finally, I really thank my family for allowing me to enter a doctoral course.

Appendix A

The relative nonlinearity for two pairs of random vectors of ~1.72 is described here. First, we introduce a Gaussian distribution with a mean of 0 and standard deviation σ,

$$N(0,\sigma) = \frac{1}{\sqrt{2\pi\sigma}} \exp\left(-\frac{x^2}{2\sigma^2}\right), \tag{A1}$$

and the χ^2 distributions with 1 degree of freedom,

$$\chi^2(1) = \frac{1}{\sqrt{2\pi x}} \exp\left(-\frac{x}{2}\right). \tag{A2}$$

Let x and y be an element of n-dimensional state vectors $\boldsymbol{x}$ and $\boldsymbol{y}$ followed by Gaussian distributions $N(0,a)$ and $N(0,b)$, respectively. Here, standard deviations a and b are followed by $\chi^2(1)$. Given a and b, the numerator of the relative nonlinearity for two random vectors [Eq. (3.1)] is the norm of two vectors, which is equivalent to the square of the sum of two random numbers estimated by the expectation value of $(x+y)^2$,

$$\int_{\mathbb{R}^2} (x+y)^2 \frac{1}{\sqrt{2\pi a}} \exp\left(-\frac{x^2}{2a^2}\right) \frac{1}{\sqrt{2\pi b}} \exp\left(-\frac{y^2}{2b^2}\right) dxdy = a^2 + b^2 \tag{A3}$$

The expectation value of $\|\boldsymbol{x}+\boldsymbol{y}\|^2$ is the n sum of a^2+b^2. Factor n is also in denominator $\|\boldsymbol{x}\|^2$ and $\|\boldsymbol{y}\|^2$ of the relative nonlinearity, and thus n is canceled out. Then, the expectation value of $\|\boldsymbol{x}+\boldsymbol{y}\|$ is

$$\begin{aligned} &\mathbb{E}\left[\sqrt{a^2+b^2}\right] \\ &= \int_0^\infty \int_0^\infty \sqrt{a^2+b^2} \frac{1}{\sqrt{2\pi a}} e^{-\frac{a}{2}} \frac{1}{\sqrt{2\pi b}} e^{-\frac{b}{2}} dadb \sim 1.71969, \end{aligned} \tag{A4}$$

which is nearly $\sqrt{3} \sim 1.73205$ (Hohenegger and Schär 2007a).

References

Ancell BC, Mass CF (2006) Structure, growth rates, and tangent linear accuracy of adjoint sensitivities with respect to horizontal and vertical resolution. Mon. Wea Rev., 134:2971–2988. doi:10.1175/MWR3227.1.

Beljaars ACM, Holtslag AAM (1991) Flux parameterization over land surfaces for atmospheric models. J. Appl. Meteor., 30:327–341. doi:10.1175/1520-0450(1991)030<0327:FPOLSF>2.0.CO;2.

Bierdel L, Selz T, Craig G (2017) Theoretical aspects of upscale error growth through the mesoscales: An analytical model. Quart. J. Roy. Meteor. Soc., 143:3048–3059. doi:10.1002/qj.3160.

Bierdel L, Selz T, Craig GC (2018) Theoretical aspects of upscale error growth on the mesoscales: Idealised numerical simulations. Quart. J. Roy. Meteor. Soc., 144:682–694. doi:10.1002/qj.3236.

Bonavita M, Lean P, Holm E (2018) Nonlinear effects in 4D-VAR. Nonlin. Processes Geophys., 25:713–729, doi:10.5194/npg-25-713-2018.

Charney JG, Fjortoft R, von Neumann J (1950) Numerical integration of the barotropic equation. Tellus, 2:237–254, doi.:10.1111/j.2153-3490.1950.tb00336.x.

Demirdjian R., Doyle JD, Reynolds CA, Norris JR, Michaelis AC, Ralph FM (2020) A case study of the physical processes associated with the atmospheric river initial-condition sensitivity from an adjoint model. J. Atmos. Sci., 77:691–709. doi:10.1175/JAS-D-19-0155.1.

Duc L, Kawabata T, Saito K, Oizumi T (2021) Forecasts of the July 2020 Kyushu heavy rain using a 1000-member ensemble Kalman filter. SOLA, 17:41–47. doi:10.2151/sola.2021-007.

Durran DR, Weyn JA (2016) Thunderstorms do not get butterflies. Bull. Amer. Meteor. Soc., 97:237–243, doi:10.1175/BAMS-D-15-00070.1.

Ehrendorfer M, Errico RM, Raeder KD (1999) Singular-vector perturbation growth in a primitive equation model with moist physics. J. Atmos. Sci., 56:1627–1648. doi:10.1175/1520-0469(1999)056<1627:SVPGIA>2.0.CO;2.

Epstein ES (1969) Stochastic-dynamic prediction. Tellus, 21:739–759. doi:10.1111/j.2153-3490.1969.tb00483.x.

Gill AE (1982) Atmosphere-ocean dynamics. Academic Press, 680pp.

Gilmour I, Smith LA, Buizza R (2001) Linear regime duration: Is 24 hours a long time in synoptic weather forecasting? J. Atmos. Sci., 58:3525–3539. doi:10.1175/1520-0469(2001)058<3525:LRDIHA>2.0.CO;2.

Haiden T, Janousek M, Vitart F, Ben-Bouallegue Z, F Prates (2023) Evaluation of ECMWF forecasts, including the 2023 upgrade. ECMWF Technical Memorandum, 911, 60pp.

Hara T, (2015) Necessity of parameterizations for convective initiation in high resolution cloud-permitting models. CAS/JSC WGNE Res. Activ. Atmos. Oceanic Modell., 45:04.06–04.07.

Hirockawa Y, Kato T, Tsuguti H, Seino N (2020) Identification and classification of heavy rainfall areas and their characteristic features in Japan. J. Meteor. Soc. Japan, 98:835−857. doi:10.2151/jmsj.2020-043.

Hoffman RN, Kalnay E (1983) Lagged average forecasting, an alternative to Monte Carlo forecasting. Tellus, 35A:100–118. doi:10.1111/j.1600-0870.1983.tb00189.x.

Hohenegger C, Schär C (2007a) Predictability and error growth dynamics in cloud-resolving models. J. Atmos. Sci., 64:4467–4478. doi:10.1175/2007JAS2143.1.

Hohenegger C, Schär C (2007b) Atmospheric predictability at synoptic versus cloud-resolving scales. Bull. Amer. Meteor. Soc., 88:1783–1793. doi:10.1175/BAMS-88-11-1783.

Ikawa M. Saito K (1991) Description of a non-hydrostatic model developed at the Forecast Research Department of the MRI. Tec. Rep. MRE., 28, 238 pp.

Ikuta Y, Fujita T, Ota Y, Honda Y (2021) Variational data assimilation system for operational regional models at Japan meteorological agency. J. Meteor. Soc. Japan, 99:1563–1592. doi:10.2151/jmsj.2021-076.

Ishida J, Aranami K, Kawano K, Matsubayashi K, Kitamura Y, Muroi C (2022) ASUCA: the JMA operational non-hydrostatic model. J. Meteor. Soc. Japan, 100:825–846. doi:10.2151/jmsj.2022-043.

Japan Meteorological Agency (2022) Outline of the operational numerical weather prediction at the Japan Meteorological Agency. Appendix to WMO Tech. Progress Rep. on the Global Data-processing and Forecasting System and Numerical Weather Prediction, Tokyo, Japan Meteorological Agency, accessed 20 May 2024 [Available at https://www.jma.go.jp/jma/jma-eng/jma-center/nwp/outline2022-nwp/index.htm]

Johnson A, Wang X, (2016) A study of multiscale initial condition perturbation methods for convective-permitting ensemble forecasts. Mon. Wea. Rev., 144:2579–2604. doi: 10.1175/MWR-D-16-0056.1.

Kain JS, Fritsch JM (1990) A one-dimensional entraining/detraining plume model and its application in convective parameterization. J. Atmos. Sci., 47:2784–2802. doi:10.1175/1520-0469(1990)047<2784:AODEPM>2.0.CO;2.

Kain, JS, (2004) The Kain-Fritsch convective parameterization: An update. J. Appl. Meteor., 43, 170–181. doi:10.1175/1520-0450(2004)043%3C0170:TKCPAU%3E2.0.CO;2.

Kalnay E (2002) Atmospheric modeling, data assimilation and predictability. Cambridge University Press, 368pp.

Kato T (2020) Quasi-stationary band-shaped precipitation systems, named "senjo-kousuitai," causing localized heavy rainfall in Japan. J. Meteor. Soc. Japan, 98:485–509. doi:10.2151/jmsj.2020-029.

Kawano T, Kawamura R (2020) Genesis and maintenance processes of a quasi-stationary convective band that produced record-breaking precipitation in northern Kyushu, Japan on 5 July 2017. J. Meteor. Soc. Japan, 98:673−690. doi:10.2151/jmsj.2020-033.

Kühnlein C, Keil C, Craig GC, Gebhardt C (2014) The impact of downscaled initial condition perturbations on convective-scale ensemble forecasts of precipitation. Quart. J. Roy. Meteor. Soc., 140:1552–1562. doi:10.1002/qj.2238.

Kusabiraki H, Kitamura Y, Sawada M, Matsubayashi K, Nishimoto S (2021) Increasing Vertical Resolution and Updating Physical Processes in JMA's Regional NWP System. CAS/JSC WGNE Res. Activ. Atmos. Oceanic Modell., 51:05.07–05.08.

Lang STK, Jones SC, Leutbecher M, Peng MS, Reynolds CA (2012) Sensitivity, structure, and dynamics of singular vectors associated with Hurricane Helene (2006). J. Atmos. Sci., 69:675–694, doi:10.1175/JAS-D-11-048.1.

Leith CE, (1974) Theoretical skill of Monte Carlo forecasts. Mon. Wea. Rev. 102:409–418.

doi:10.1175/1520-0493(1974)102%3C0409:TSOMCF%3E2.0.CO;2.

Lin YH, Farley RD, Orville HD (1983) Bulk parameterization of the snow field in a cloud model. J. Clim. Appl. Meteor., 22:1065–1092. doi:10.1175/1520-0450(1983)022%3C1065:BPOTSF%3E2.0.CO;2.

Lorenz EN, (1963) Deterministic nonperiodic flow. J. Atmos Sci. 20:130-141. doi:10.1175/1520-0469(1963)020<0130:DNF>2.0.CO;2.

Lorenz EN (1965) A study of the predictability of a 28-variable atmospheric model. Tellus 17:321–333. doi:10.1111/j.2153-3490.1965.tb01424.x.

Milan M, and Coauthors (2020) Hourly 4D-Var in the Met Office UKV operational forecast model. Quart. J. Roy. Meteor. Soc., 146:1281–1301. doi:10.1002/qj.3737.

Minamide M, Zhang F, Clothiaux EE (2020) Nonlinear forecast error growth of rapidly intensifying Hurricane Harvey (2017) examined through convection-permitting ensemble assimilation of GOES-16 all-sky radiances. J. Atmos. Sci., 77:4277–4296. doi:10.1175/JAS-D-19-0279.1.

Nakanishi M, Niino H (2009) Development of an improved turbulence closure model for the atmospheric boundary layer. J. Meteor. Soc. Japan, 87:895–912. doi:10.2151/jmsj.87.895.

Oizumi T, Satio K, Duc L, Ito J (2020) Ultra-high resolution numerical weather prediction with a large domain using the K Computer. Part 2: The case of the Hiroshima heavy rainfall event on August 2014 and dependency of simulated convective cells on model resolutions. J. Meteor. Soc. Japan, 98:1163–1182. https://doi.org/10.2151/jmsj.2020-

060.

Ono K, Kunii M, Honda Y (2021) The regional model-based Mesoscale Ensemble Prediction System, MEPS, at the Japan Meteorological Agency. Quart. J. Roy. Meteor. Soc., 147:465–484. doi:10.1002/qj.3928.

Persson A (2005) Early operational numerical weather prediction outside the USA: an historical introduction. Part 1: Internationalism and engineering NWP in Sweden, 1952-69. Meteorol. Appl. 12:135-159. doi:10.1017/S1350482705001593

Raynaud L, Bouttier F (2017) The impact of horizontal resolution and ensemble size for convective-scale probabilistic forecasts. Quart. J. Roy. Meteor. Soc., 143:3037–3047. doi:10.1002/qj.3159.

Rodwell M, and Coauthors (2013) Characteristics of occasional poor medium-range weather forecasts for Europe. Bull. Amer. Meteor. Soc., 94:1393–1405. doi:10.1175/BAMS-D-12-00099.1.

Sawada K, Honda Y (2021) A constraint method for supersaturation in a variational data assimilation system. Mon. Wea. Rev., 149:3707–3724. doi:10.1175/MWR-D-20-0357.1.

Sawada M, Kitamura Y, Matsubayashi K, Kusabiraki H, Nishimoto S, Aikawa T, Yamasaki Y (2022) Extending forecast range and introducing an ocean mixed layer model in JMA's Mesoscale NWP system. CAS/JSC WGNE Res. Activ. Atmos. Oceanic Modell., 52:05.07–05.08.

Schwartz CS, Poterjoy J, Romine GS, Dowell DC, Carley JR, Bresch J (2022) Short-term convection-allowing ensemble precipitation forecast sensitivity to resolution of initial condition perturbations and central initial states. Wea. Forecasting, 37:1259–1286. doi:

10.1175/WAF-D-21-0165.1.

Selz T, Craig GC (2015) Upscale error growth in a high-resolution simulation of a summertime weather event over Europe. Mon. Wea. Rev., 143:813–827. doi:10.1175/MWR-D-14-00140.1.

Sun YQ, Zhang F (2016) Intrinsic versus practical limits of atmospheric predictability and the significance of the butterfly effect. J. Atmos. Sci., 73:1419–1438. doi:10.1175/JAS-D-15-0142.1.

Toth Z, Kalnay E (1993) Ensemble forecasting at NMC: The generation of perturbation. Bull. Amer. Meteor. Soc., 74:2317–2330. doi: 10.1175/1520-0477(1993)074,2317:EFANTG.2.0.CO;2.

Toth Z, Kalnay E (1997) Ensemble forecasting at NCEP: the breeding method. Mon. Wea. Rev. 125:3297–3318. doi:org/10.1175/1520-0493(1997)125%3C3297:EFANAT%3E2.0.CO;2.

Wang Y, Bellus M, Geleyn JF, Ma X, Tian W, Weidle F (2014) A new method for generating initial condition perturbations in a regional ensemble prediction system: blending. Mon. Wea. Rev., 142:2043–2059. doi:10.1175/MWR-D-12-00354.1.

Weyn JA, Durran DR (2017) The dependence of the predictability of mesoscale convective systems on the horizontal scale and amplitude of initial errors in idealized simulations. J. Atmos. Sci., 74:2191–2210. doi:10.1175/JAS-D-17-0006.1.

Wu PY, Takemi T (2023) Impacts of mountain topography and background flow conditions on the predictability of thermally induced thunderstorms and the associated error growth. J. Atmos. Sci., 80:1177–1199. doi:10.1175/JAS-D-21-0331.1.

Yonehara H, Kuroki Y, Ujiie M, Matsukawa C, Kanehama T, Nagasawa R, Ochi K, Higuchi M, Ichikawa Y, Sekiguchi R, Hirahara S (2023) Upgrade of JMA's operational global numerical weather prediction system. CAS/JSC WGNE Res. Activ. Atmos. Oceanic Modell., 53: 06.15–06.16.

Zhang F, Bei N, Rotunno R, Snyder C, Epifanio CC (2007) Mesoscale predictability of moist baroclinic waves: convection-permitting experiments and multistage error growth dynamics. J. Atmos. Sci., 64, 3579–3594. doi:10.1175/JAS4028.1.